Volume 17, Issue 3, 172519 (1-27)

Iranian Journal of Earth Science (IJES)

https://doi.org/10.57647/j.ijes.2025.16784

Geodynamic and source characterization of intrusive rocks from Nusha: A key to Neothetyan arc related tectonomagmatic evolution of Central Alborz

Farbood Hakimi Bandboon[1], Saeed Taki[1,*], Mohammad Modarresnia[2]

[1]*Department of Geology, Faculty of Basic Sciences, La.C., Islamic Azad University, Lahijan, Iran.*
[2]*Faculty of Basic Sciences, Ra.C., Islamic Azad University, Rasht, Iran.*

[*]**Corresponding author:** saeed.taki@iau.ac.ir

Original Research

Received:
12 January 2024
Revised:
10 March 2024
Accepted:
28 April 2024
Published online:
10 July 2025

Abstract:

Nusha intrusive rocks south of Ramsar (N Iran) include gabbronorites, gabbros, monzogabbros, diorites, syenites, monzonites, monzodiorites, granodiorites, and quartz monzonite with Eocene age (56 ± 2 Ma). Electron probe micro analyzing (EPMA) on clinopyroxene, orthopyroxene and biotite of these rocks reveals that they are compositionally augite to salite, hypersthene, and Mg biotite to phlogopite, respectively. Geothermometry and Geobarometry calculations based on CPX compositions correspond to temperatures of approximately 1170 to 1210 °C and mostly 6 to 7 kb pressure. Whole-rock geochemistry indicates that nearly all rocks are high-K calc-alkaline to shoshonitic in nature and display continental arc-related geochemical characteristics, with enrichment in LILE and LREE and low concentration in HFSE and HREE, along with Nb, Ta and Ti negative anomalies. The positive anomaly of Pb, and K, and the relatively low Ce/Yb and Nb/U ratios suggest crustal contamination. Nb/La ratios mostly between 0.4 and 1.34, as well as Nb/Zr ratio (0.76) indicate a lithospheric mantle origin. Trace-element ratios, when compared with experimental studies, point to an enriched lithospheric mantle source composed of spinel-garnet lherzolite, which underwent a relatively low degree of partial melting ($3-20\%$) to produce the Nusha intrusions.

Keywords: Intrusive rocks; High-K calc-alkaline; Nusha; Central Alborz

1. Introduction

The Nusha magmatic rocks are structurally situated within the central Alborz zone (Alavi, 1996), which forms part of the Alborz-Azerbaijan magmatic belt (Nabavi, 1976). The Alborz mountain range has been affected by the Alpine-Himalayan orogeny, and igneous activity in this zone occurred during the Paleozoic, Mesozoic, and Cenozoic eras, as in many parts of Iran (Darvishzadeh, 1991). Since the Late Cretaceous, igneous activity in Alborz magmatic belt has intensified, continuing into the Quaternary (Alavi, 1996), with major activity during the Late Cretaceous, Eocene, Miocene, and Quaternary periods (Mollai et al., 2021; Azizi and Tsuboi, 2021).

In the Alborz-Azerbaijan magmatic belt, various extrusive, hypabyssal, and plutonic rocks formed from the Paleocene to Oligocene in this area. Many of these intrusive rocks are high potassium calc-alkaline to shoshonite (Foley and Peccerillo, 1992; Turner et al., 1996; Aghazadeh, 2009; Mokhtari et al., 2010; Taki, 2011; Aghazadeh et al., 2013; Nabatian et al., 2014; Bahajroy et al., 2022; Arjmandzadeh et al., 2022; Nazari et al., 2023; Ousta et al., 2024; Abdolahadi et al., 2025; Salehpour et al., 2025). Whole-rock geochemistry of igneous rocks west of Alborz-Azerbaijan magmatic belt (AMB) suggests they parent magmas formed due to subduction of the Neo-Tethys oceanic lithosphere beneath Iran's microplate during the Tertiary (e.g. (Asiabanha et al., 2009; Asiabanha and Foden, 2012; Dabiri et al., 2018; Ghasempour et al., 2014; Nabatian et al., 2014; Ashrafi et al., 2024)). There is limited information about geochemical nature and the genesis of Nusha intrusive rocks based on the whole-rock and especially the microprobe data. In this study, we aim to determine the geochemical nature of Nusha area's intrusive rocks using whole-rock and mineral composition results to identify their tectonomagmatic setting and origin.

2. Geological setting

The study area is located approximately 30 kilometers south of Ramsar in Mazandaran province, between the eastern longitudes of 50° 36′ to 50° 40′ and northern latitudes of 36° 32′ to 36° 37′. Structurally, it lies within the Central Alborz subzone (Alavi, 1996). The intrusive bodies in this area are exposed along a west-northwest trending belt formed by post-Cretaceous fractures (Annells et al., 1975). In addition to the intrusive rocks, sedimentary rock formations of various ages are exposed, including the Mila (Cambrian), Mobarak (lower Carboniferous), Dorud (Lower Permian), Ruteh (Upper Permian), Nesen (Upper Permian), Elika (Lower-Middle Triassic), Shemshak (Upper Triassic-lower Jurassic) formations, as well as carbonate and volcanic rocks from the late Cretaceous formations (Baharfiruzi et al., 2001) (Figs. 1 (a) and 1 (b)).

The granitoid intrusions in the Ramsar geological sheet can be divided into two categories (Fig. 1 (a)). The first has northwest-southeast trend (Baharfiruzi et al., 2001) and intruded into Shemshak formation during the Eocene (56 ± 2 Ma) (Nusha type granitoids), with cooling lasting until about 25 Ma (Axen et al., 2001). The second set, with a north-south trend (Baharfiruzi et al., 2001) and intruded into Paleozoic and Mezozoic formations about 6.8 ± 0.1 Ma (Arood granitoids type) (Axen et al., 2001). The Nusha granitoid outcrop starts from the western slope of the Se-Hazar valley and extends northwestward to the southwest of the Nusha village (Yazdi et al., 2016; Axen et al., 2001). This unit is divided into two masses by a right-lateral strike-slip fault. The southern boundary is completely faulted, with the Upper Paleozoic assemblage thrust over the mass. Annells et al. (1975) considered the contact between these granitoids and the Cretaceous volcanic rocks in southwest Nusha as normal, consistent with post-Cretaceous age determination data (Axen et al., 2001).

3. Methodology

After sampling and petrographic studies of intrusive rocks in the Nusha area, 27 representative samples were sent to Actlabs (in Canada) and Zarazma (in Iran) companies for whole-rock chemical analysis. The ICP-AES method was used to evaluate major and some minor elements (Table 1), while rare earth and refractory elements were measured using ICP-MS (Table 1). Since Fe was reported as total

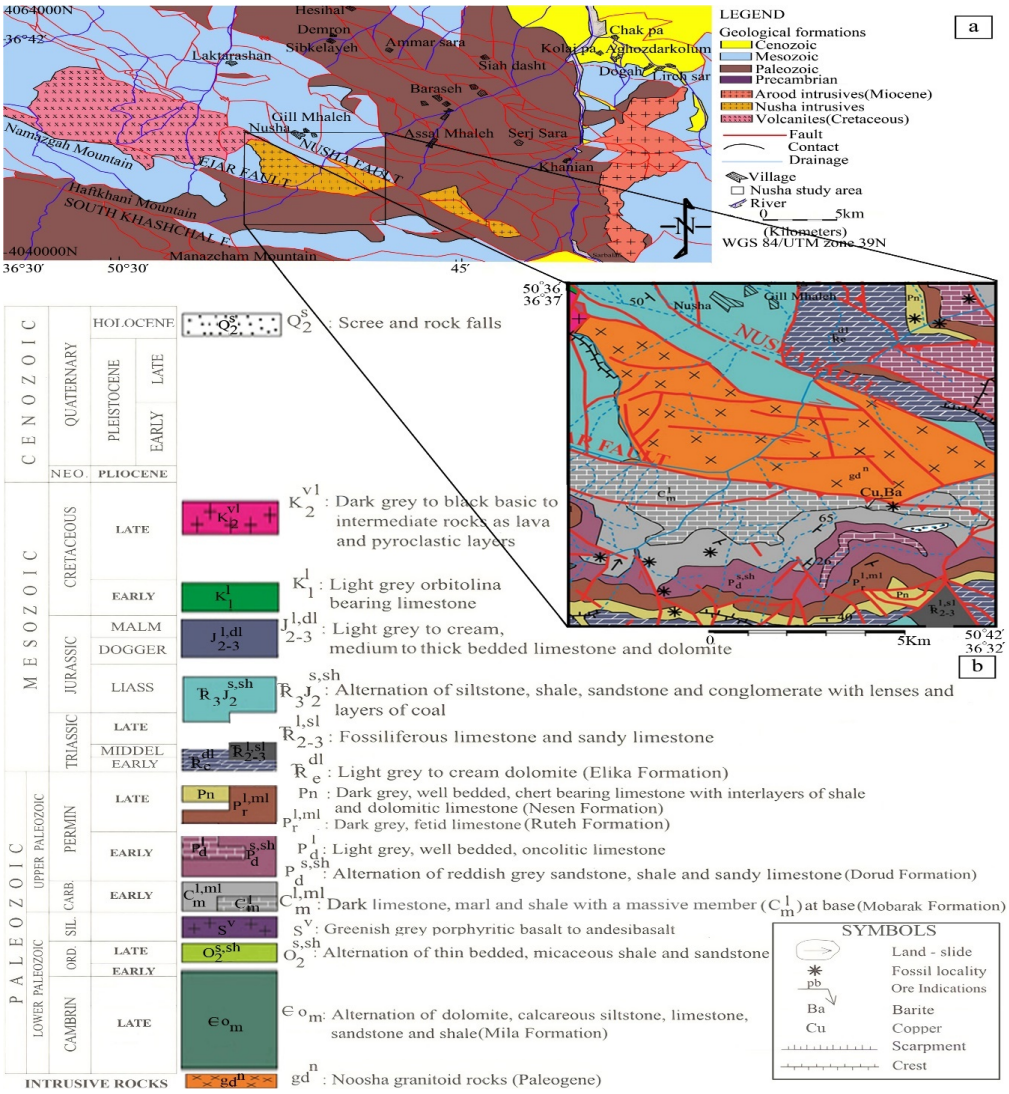

Figure 1. (a) Simplified geological map of the southern part of Ramsar displaying, (b) The Nusha region (black square) in greater detail.

Table 1. Whole-rock chemical analysis results for representative samples from the study area, obtained from Zarazma (Iran) and Actlabs (Canada) (indicated by *). Major oxides are reported in percentage, while minor and trace elements are in ppm. Elemental ratios and indices are also included.

Sample no	2	3	4	5	6	7	8	9
SiO_2	53.1	68.23	60.99	55.9	50.53	63.17	48.63	50.54
TiO_2	0.9	0.28	0.93	0.65	1.59	0.54	1.16	1.99
Al_2O_3	17.99	15.05	15.94	19.28	17.45	17.12	17.61	15.11
Fe_2O_3*	8.4	2.75	6.2	6.11	10.3	4.8	8.89	14.26
MnO	0.19	0.06	0.15	0.13	0.17	0.16	0.16	0.33
MgO	2.22	0.56	1.88	2.8	4.49	1.09	5.82	2.71
CaO	7.83	1.96	4.93	6.33	9	3.21	9.34	6.55
Na_2O	5.04	3.98	3.45	4.11	3.22	4.37	2.77	4.31
K_2O	1.49	5.32	2.81	2.26	1.57	4.18	1.64	2.52
P_2O_5	0.48	0.06	0.28	0.36	0.25	0.17	0.14	0.66
LOI	2.24	1.64	2.37	2.01	1.38	1.1	3.73	0.73
Total	99.99	100	100.06	100.08	99.88	100.05	99.72	99.93
Sc	6.1	2.7	14.2	5.1	20.1	4.3	26.7	7.7
V	99	18	46	80	205	38	183	68
Co	14.6	2.4	6.8	15.6	27.9	7	28.1	19.4
Cs	0.5	2.5	0.6	0.5	1.1	2.1	0.7	1
Rb	42	257	107	85	71	152	61	84
Ba	300	399	584	626	191	702	234	909
Sr	782	191	238	491	379	248	365	761
Y	19.6	21.1	26.6	10.9	16.3	19.2	13.8	29.3
Ta	1.18	1.75	0.82	0.44	0.61	1.59	0.83	1
Zr	11	29	31	6	41	11	16	30
Nb	16.2	21.3	13.7	10.8	10	26	13.4	24.5
Hf	1.39	2.48	2.45	1.12	2.67	1.52	1.79	2.82
Pb	4	4	3	5	16	7	11	36
La	23	41	28	21	13	30	10	58
Ce	42	71	54	34	25	53	18	108
Pr	7.46	8.82	7.68	6.49	5.93	8.06	4.86	14.03
Nd	28.6	31.3	31.2	23.5	22.9	28.8	17.6	56
Sm	6.18	6.1	7.62	5.77	4.9	6.42	4.12	12.09
Eu	2.02	1.43	2.32	2.3	1.6	2.14	1.06	4.53
Gd	3.89	4.35	4.5	3.25	3.28	3.97	2.56	7.54
Tb	0.7	0.73	0.85	0.49	0.57	0.66	0.46	1.34
Dy	3.18	3.39	3.96	2.28	2.77	3.19	2.29	4.89
Ho	-	-	-	-	-	-	-	-
Er	2.45	2.52	2.9	1.68	1.87	2.33	1.62	3.52
Tm	0.3	0.41	0.4	0.2	0.27	0.36	0.24	0.47
Yb	1.9	2.1	2.2	1.1	1.9	2	1.7	2.7
Lu	0.39	0.5	0.44	0.31	0.33	0.48	0.3	0.51
Th	9.58	24.9	10.89	9.29	10.58	13.98	6.27	10.73
U	1.4	3	1.1	1.2	1.2	2.7	0.6	1.7
Be	1	3.2	1.4	1.3	0.6	1.7	0.5	1.3
Ga	-	-	-	-	-	-	-	-
Sn	3.1	3.9	4.8	3.6	3.6	5	2.4	4.9
W	1.4	3.1	1	1	1	2	1	1
Mo	0.1	1	0.1	0.1	0.1	1	0.1	1
Cu	26	24	12	26	65	15	24	24
Zn	51	29	68	50	80	64	63	138
As	5.8	7.5	7.3	5.5	7.9	6.5	4.8	9.7
Ge	-	-	-	-	-	-	-	-
Li	8	7	13	9	17	16	13	11
Bi	0.1	0.1	0.1	0.1	0.1	0.1	0.1	0.1
Ta/Nb	0.07	0.08	0.05	0.04	0.06	0.06	0.06	0.04
K/Rb	252.8	141.36	191.35	187.96	161.08	181.91	187.63	216.9
Rb/Sr	0.05	1.34	0.44	0.17	0.18	0.61	0.16	0.11
Rb/Ba	0.14	0.64	0.18	0.13	0.37	0.21	0.26	0.09
Zr/Hf	7.91	11.69	12.65	5.35	15.35	7.23	8.93	10.63
Sm/Eu	3.05	4.26	3.28	2.5	3.06	3	3.88	2.66
Ce/Yb	22.1	33.8	24.54	30.9	13.15	26.5	10.58	40
La/Yb	12.10	19.52	12.72	19.09	6.84	15	5.88	21.48
Eu/Eu*	1.25	0.84	1.21	1.63	1.21	1.29	0.99	1.44

Continued of Table 1.

Sample no	10	12	14	16	17	18	19	22
SiO_2	50.35	64.39	45.31	61.87	52.4	60.33	48.05	68.69
TiO_2	1.16	0.53	1.75	0.68	1.1	0.71	0.85	0.36
Al_2O_3	17.47	16.22	15.09	16.91	15.68	17.18	15.57	14.99
Fe_2O_3*	8.96	5.57	10.78	5.58	8.27	5.76	10.38	3.23
MnO	0.24	0.17	0.16	0.13	0.14	0.22	0.18	0.06
MgO	5.35	1.02	10.33	1.57	5.72	2.05	9.12	0.67
CaO	8.97	4.06	10.78	3.69	9.92	4.46	8.94	1.92
Na_2O	2.55	3.6	1.93	4.22	2.57	3.88	2.22	4.14
K_2O	2.46	2.79	0.98	3.36	1.93	3.79	1.37	4.92
P_2O_5	0.17	0.24	0.17	0.25	0.14	0.16	0.31	0.11
LOI	2.23	1.28	2.66	1.63	2.07	1.3	2.87	0.87
Total	100.07	100	100.07	100	100.06	100	99.99	100.06
Sc	27	8.1	38.9	6.5	21.6	8.2	21.7	3.2
V	203	10	258	54	201	78	156	24
Co	25.9	3.9	46.6	10.2	29.6	13	38	4.3
Cs	3.6	1.2	0.5	2.1	3.7	1.6	<0.5	3
Rb	146	62	50	130	98	125	50	196
Ba	341	550	169	381	159	632	214	415
Sr	301	277	419	333	284	350	322	160
Y	16.4	26.7	17.6	23.2	17	19.4	12.2	21.9
Ta	0.9	0.78	0.43	1.6	0.68	1.29	0.61	0.79
Zr	25	16	59	10	26	13	52	17
Nb	12.8	10.2	8.8	26.2	10.4	22.9	10	19.1
Hf	1.98	1.6	2.63	1.28	2.05	1.33	2.41	1.6
Pb	21	4	11	11	10	43	3	7
La	12	22	16	47	15	31	12	32
Ce	22	46	29	80	27	51	24	58
Pr	5.17	7.59	5.58	10.54	5.55	7.1	5.09	7.09
Nd	19.5	31.3	22.3	40.5	21	25.8	18.6	24
Sm	4.44	7.51	4.51	7.86	4.33	5.75	3.73	5.09
Eu	1.43	2.24	1.38	1.82	1.12	1.83	1.1	1.13
Gd	2.85	4.48	3.26	5.65	3.06	3.33	2.58	3.29
Tb	0.49	0.88	0.6	0.92	0.5	0.54	0.37	0.56
Dy	2.59	3.76	2.85	4.01	2.63	2.5	1.93	2.74
Ho	-	-	-	-	-	-	-	-
Er	1.93	2.8	2.02	2.98	1.94	1.97	1.43	2.29
Tm	0.25	0.37	0.26	0.4	0.27	0.29	0.18	0.36
Yb	1.9	2.1	2	2.2	2.1	1.9	1.5	2.3
Lu	0.31	0.42	0.33	0.54	0.36	0.35	0.23	0.48
Th	8.83	10.37	6.63	17.46	10.42	13.86	6.06	21.24
U	1.2	0.9	0.6	3.3	1.1	2.1	0.4	4.8
Be	0.7	1.5	0.5	2.2	1	1.7	0.5	3.3
Ga	-	-	-	-	-	-	-	-
Sn	3.7	2.8	2.7	5.5	3.1	4.6	2.6	4.1
W	2.4	1.2	1	1.7	1.6	1.9	1	1.1
Mo	0.1	0.1	0.1	0.1	0.1	0.1	0.1	1
Cu	64	14	51	15	188	32	45	14
Zn	101	73	70	49	44	133	64	23
As	9.6	8.6	6.1	7.6	8.2	8.1	4.5	7.7
Ge	-	-	-	-	-	-	-	-
Li	48	14	13	13	38	15	13	9
Bi	0.1	0.1	0.1	0.1	0.1	0.1	0.1	0.1
Ta/Nb	0.07	0.07	0.04	0.06	0.06	0.05	0.06	0.04
K/Rb	123.04	326.14	159.76	177.13	141.21	214.62	190.48	174.68
Rb/Sr	0.48	0.22	0.11	0.39	0.34	0.35	0.15	1.22
Rb/Ba	0.42	0.11	0.29	0.34	0.61	0.19	0.23	0.47
Zr/Hf	12.62	10	22.43	7.81	12.68	9.77	21.57	10.62
Sm/Eu	3.1	3.35	3.26	4.31	3.86	3.14	3.39	4.5
Ce/Yb	11.57	21.9	14.5	36.36	13.17	26.84	16	25.21
La/Yb	6.31	10.47	8	21.36	7.14	16.31	8	13.91
Eu/Eu*	1.22	1.18	1.09	0.83	0.94	1.27	1.08	0.84

Continued of Table 1.

Sample no	27	29	30	31	23*	24*	25*	26*
SiO_2	57.70	50.66	65.63	70.05	64.5	63.61	68.93	61.78
TiO_2	0.50	1.31	0.51	0.31	0.582	1.124	0.394	0.757
Al_2O_3	16.23	16.25	16.60	14.74	16.87	16.19	14.62	17.24
Fe_2O_3*	8.93	9.24	3.72	2.71	4.34	5.42	3.2	5.7
MnO	0.15	0.16	0.09	0.07	0.115	0.070	0.072	0.131
MgO	0.15	6.16	1.02	0.51	0.86	1.57	0.78	1.53
CaO	12.19	10.38	2.04	1.74	2.68	3.53	2.03	3.91
Na_2O	1.30	2.52	4.63	3.49	4.63	3.80	4.00	4.66
K_2O	1.16	1.49	4.63	5.41	4.65	3.60	4.65	3.56
P_2O_5	0.14	0.13	0.13	0.08	0.18	0.29	0.10	0.21
LOI	1.32	1.63	0.87	0.83	0.93	1.03	0.69	1.12
Total	99.92	100.04	99.99	100.05	100.3	100.2	99.47	100.6
Sc	4.4	33.5	5.8	3.1	5	9	4	8
V	90	257	38	22	24	96	34	70
Co	3.9	32.7	5.7	4.3	6	12	6	9
Cs	0.5	1.4	1	2.5	1.0	2.7	2.3	1.0
Rb	22	41	85	193	95	120	186	89
Ba	114	212	671	544	904	427	504	740
Sr	1401	377	307	228	286	393	220	396
Y	20	19.7	25.1	17.6	21	23	24	28
Ta	0.91	0.89	1.05	1.5	2.5	3.7	4.3	2.4
Zr	16	31	12	8	262	137	175	303
Nb	15.7	10.9	16.6	21.5	27	37	34	31
Hf	1.34	2.13	1.19	1.3	5.1	3.9	4.1	6.2
Pb	9	7	6	13	10	7	7	10
La	23	16	41	24	41.2	44.6	43.5	40.0
Ce	40	29	71	40	71.3	81.3	75.6	75.6
Pr	5.96	4.89	6.1	6.47	6.88	8.33	7.09	7.92
Nd	20.7	17.6	21.6	24.1	24.7	29.9	23.5	29.8
Sm	3.96	3.74	4.87	5.34	4.4	5.4	4.1	5.9
Eu	1.39	0.96	1.27	1.77	1.59	1.41	0.82	1.46
Gd	2.96	2.59	3.18	3.19	3.8	5.0	3.5	4.8
Tb	0.44	0.44	0.49	0.56	0.6	0.7	0.5	0.8
Dy	2.33	2.18	2.33	2.55	3.5	4.3	3.3	4.4
Ho	-	-	-	-	0.7	0.8	0.6	0.9
Er	1.7	1.64	1.76	1.88	2.0	2.3	2.1	2.6
Tm	0.26	0.21	0.24	0.31	0.31	0.33	0.34	0.41
Yb	2.2	2.4	2.5	1.8	2.3	2.4	2.4	2.8
Lu	0.32	0.3	0.33	0.38	0.36	0.38	0.41	0.46
Th	10.12	8.22	14.41	15.89	15.8	20.8	26.7	15.5
U	1.9	0.8	2.6	3.2	3.1	5.5	6.1	3.7
Be	1.7	0.8	2.4	1.8	2	3	4	3
Ga	-	-	-	-	-	-	-	-
Sn	3.3	1.6	1.7	3.8	2	2	2	2
W	1.2	1	1	1.3	2	1	1	1
Mo	0.1	0.1	0.1	0.1	2	2	2	2
Cu	18	129	11	63	30	60	30	20
Zn	24	78	68	65	60	60	30	80
As	6.1	7.7	9.4	9.4	5	5	5	5
Ge	-	-	-	-	2	1	1	2
Li	4	14	6	8	-	-	-	-
Bi	0.1	0.1	0.1	0.1	0.4	0.4	0.4	0.4
Ta/Nb	0.05	0.08	0.06	0.06	0.09	0.1	0.12	0.07
K/Rb	416	299.7	430.63	222.21	406	249	207	332
Rb/Sr	0.01	12.08	0.27	0.84	0.33	0.31	0.85	0.22
Rb/Ba	0.19	0.19	0.12	0.35	0.10	0.28	0.36	0.12
Zr/Hf	11.94	14.55	10.08	6.15	51.37	35.12	42.68	48.87
Sm/Eu	2.84	3.89	3.83	3.01	2.77	3.83	5	4.04
Ce/Yb	18.18	12.08	28.4	22.22	31	33.87	31.5	27
La/Yb	10.45	6.66	16.4	13.33	17.91	18.58	18.12	14.28
Eu/Eu*	1.24	0.94	0.98	1.31	1.18	0.82	0.66	0.83

Continued of Table 1.

Sample no	33*	34*	35*
SiO_2	50.79	60.51	48.34
TiO_2	1.618	0.762	1.232
Al_2O_3	15.97	16.08	15.35
Fe_2O_3*	9.68	4.24	10.16
MnO	0.170	0.081	0.165
MgO	6.61	1.61	8.52
CaO	8.63	4.33	10.32
Na_2O	3.06	3.68	2.17
K_2O	2.90	7.29	1.71
P_2O_5	0.25	0.23	0.17
LOI	1.03	1.78	1.46
Total	100.7	100.6	99.60
Sc	26	7	33
V	244	52	233
Co	37	17	46
Cs	3.4	1.9	2.3
Rb	115	155	71
Ba	349	1225	240
Sr	395	319	430
Y	22	25	15
Ta	1.4	2.8	1.2
Zr	143	366	101
Nb	19	38	14
Hf	3.6	7.3	2.9
Pb	5	33	5
La	23.2	36.1	16.9
Ce	47.3	68.9	34.4
Pr	5.46	7.16	4.12
Nd	22.2	25.4	16.8
Sm	5.1	4.7	3.9
Eu	1.65	1.36	1.21
Gd	5	4.1	3.6
Tb	0.7	0.6	0.6
Dy	4.2	3.8	3.4
Ho	0.8	0.8	0.6
Er	2.3	2.5	1.8
Tm	0.35	0.36	0.25
Yb	2.2	2.4	1.7
Lu	0.34	0.42	0.26
Th	5.5	12.3	5
U	1.5	3.6	1.5
Be	2	2	1
Ga	-	-	-
Sn	2	2	1
W	1	3	1
Mo	2	4	2
Cu	80	120	40
Zn	90	90	70
As	5	6	5
Ge	2	1	1
Li	-	-	-
Bi	0.4	0.4	0.4
Ta/Nb	0.07	0.07	0.08
K/Rb	209	390	200
Rb/Sr	0.29	0.03	0.17
Rb/Ba	0.32	0.12	0.29
Zr/Hf	39.72	3.42	34.83
Sm/Eu	3.09	3.45	3.22
Ce/Yb	21.5	28.7	20.23
La/Yb	10.54	15.04	9.94
Eu/Eu*	0.99	0.94	0.98

iron, the Irvine and Baragar (1971) method was used to discriminate divalent and trivalent iron. For mineral composition, 7 samples with various lithologies were sent to the University of Oklahoma for chemical microanalysis using the Cameca SX50 electron microprobe equipped with five wavelength-dispersive spectrometers and a PGT PRISM 2000 energy-dispersive X-ray analyzer applying 20 kV acceleration, 20 nA beam current (measured at Faraday cup), and 2 μm spot size. Data from biotites, feldspars, and pyroxenes microanalysis are presented in Tables 2, 3, and 4 respectively. The Mineral Spreadsheet and Minpet 2.02 software were used to create plots and perform cation calculations.

4. Results

4.1 Petrography

The intrusive rocks in the study area include gabbronorites, gabbros, monzogabbros, diorites, syenites, monzonites, monzodiorites, granodiorites, and quartz monzonites. Detailed petrographic descriptions are provided below.

4.1.1 Gabbronorite

Gabbronorites exhibit intergranular and intersertal textures (Fig. 2 (a)). Plagioclase ($\sim$ 40 vol%) dominates, showing features like polysynthetic twinning and normal zoning. Microprobe data indicate the plagioclase core, interior, and rim compositions as bytownite, labradorite, and andesine (An_{85-39}), respectively (Fig. 3 (a)). Orthopyroxene ($\sim$ 20 vol%) and clinopyroxene ($\sim$ 5 vol%) are also present, with compositions of hypersthene and augite, respectively (Figs. 4 (a) and (b)). Biotite ($\sim$ 10 vol%) is of phlogopite type (Fe#0.32) (Figs. 5 (a1), 5 (b1), and 5 (c1)), with evidence of re-equilibration (Fig. 5 (d1)). Opaque minerals comprise $\sim$ 15 vol% of the rock. Angular spaces between plagioclase crystals are often filled with cryptocrystalline minerals ($\sim$10 vol%) (Fig. 3 (a)).

4.1.2 Gabbro

Nusha gabbros (Figs. 2 (b) and 2 (c)) exhibit wide range of mineralogy and textures, including anhedral granular, porphyritic with relatively fine-grained groundmass, poikilitic, ophitic, and intergranular textures. Plagioclase ($\sim 35-40$ vol%) dominates, with normal zoning in most porphyritic and intergranular gabbros. Microprobe data show a composition range from labradorite to andesine (An_{52-48}) in porphyritic gabbros (Fig. 3 (b)) and from anorthite to bytownite (An_{92-75}) in intergranular gabbros (Fig. 3 (c)). Clinopyroxene ($\sim$ 20 to 35 vol%) is mostly augite (Figs. 4 a, c, and d). Biotite may constitute up to about 25 vol% of the rock, and hornblende is present in some samples ($\sim$ 10 vol%), sometimes forming poikilitic structures. Opaque minerals account for less than 5% of the volume (Figs. 2 (b) and 2 (c)).

4.1.3 Monzogabbro

Monzogabbro textures vary from relatively coarse-grained anhedral granular to porphyritic with fine-grained granular groundmass. Plagioclase ($\sim$ 35 vol%) (Fig. 2 (d)) is the dominant mineral, with a microprobe composition of

Table 2. Representative electron microprobe analyses of biotites (in wt.%) from the Nusha intrusives and the calculated structural formula (in apfu) based on 11 oxygens.

Samples	1	2	3	4	5	6	7	8	9	10
SiO_2	37.75	36.81	37.70	40.95	36.52	36.71	36.49	36.16	36.55	36.52
TiO_2	5.84	5.76	5.77	3.21	6.72	6.99	4.22	4.07	4.14	4.33
Al_2O_3	12.41	12.45	12.55	11.56	13.92	13.97	15.10	14.94	14.88	14.68
Cr_2O_3	0.01	0.00	0.01	0.00	0.02	0.02	0.00	0.02	0.01	0.02
FeOt	17.10	16.99	17.28	13.95	14.18	14.23	17.15	17.38	16.77	16.92
MnO	0.09	0.09	0.07	0.09	0.12	0.09	0.35	0.34	0.32	0.32
MgO	14.55	14.20	14.17	19.12	15.08	15.39	14.24	14.30	14.28	14.38
CaO	0.01	0.00	0.02	0.05	0.04	0.03	0.03	0.04	0.04	0.01
Na_2O	0.32	0.35	0.31	0.13	0.80	0.80	0.46	0.54	0.63	0.57
K_2O	9.05	9.12	9.24	9.01	8.25	8.31	8.71	8.67	8.58	8.64
P_2O_5	0.00	0.01	0.02	0.02	0.00	0.02	0.02	0.05	0.01	0.00
NiO	0.01	0.00	0.02	0.00	0.02	0.03	0.02	0.00	0.00	0.00
F	1.97	2.08	2.20	2.60	0.63	0.50	0.20	0.28	0.17	0.21
O=F	-0.83	-0.87	-0.93	-1.09	-0.27	-0.21	-0.09	-0.12	-0.07	-0.09
Total	98.30	97.00	98.44	99.61	96.05	96.86	96.88	96.67	96.32	96.50
Si	2.85	2.83	2.86	3.01	2.72	2.71	2.71	2.71	2.73	2.73
Ti	0.33	0.33	0.33	0.17	0.37	0.38	0.23	0.23	0.23	0.24
Al	1.10	1.13	1.12	1.00	1.22	1.21	1.32	1.31	1.31	1.29
AlVI	0.11	0.11	0.14	0.18	0.20	0.16	0.43	0.40	0.44	0.39
AlIV	2.14	2.19	2.14	1.85	2.33	2.35	2.32	2.34	2.29	2.30
Fe#	0.39	0.40	0.40	0.29	0.34	0.34	0.40	0.40	0.39	0.39
Fe^{2+}	0.82	0.85	0.87	0.49	0.60	0.59	0.70	0.70	0.66	0.67
Fe^{3+}	0.10	0.07	0.07	0.13	0.22	0.24	0.22	0.23	0.23	0.23
Mg	1.64	1.63	1.60	2.10	1.67	1.69	1.58	1.59	1.59	1.60
Na	0.04	0.05	0.04	0.01	0.11	0.11	0.06	0.07	0.09	0.08
K	0.87	0.89	0.89	0.84	0.78	0.78	0.82	0.82	0.81	0.82

anorthite (An_{92}) (Fig. 3 (d)). Alkali-feldspars ($\sim$ 8 vol%) fills intergranular spaces in coarse-grained samples, while in porphyritic textures, it occurs in the groundmass. Microprobe data show microperthitic orthoclase composition ($Or_{67}Ab_{30}$) (Fig. 3 (d)). Biotite is abundant ($\sim$ 25 vol%) and of primary Mg-biotite type (Figs. 5 (a2), 5 (b2), 5 (c2), and 5 (d2)). The amount of clinopyroxene varies in different samples, from about 10 vol% in ones with relatively coarse-grained anhedral granular texture to 25 vol% in porphyritic ones. The microanalyses results show that clinopyroxene has salite and augite composition (Figs. 4 (a) and 4 (e)). Green hornblende ($\sim$ 15 vol%), opaque minerals, apatite, and sphene ($\sim$ 7 vol% total) are also present.

4.1.4 Diorite

Diorites have a relatively fine- to coarse-grained anhedral granular (Fig. 2 (e)). Plagioclase ($\sim$ 70 vol%) dominates, with an andesine (An_{38}) composition (based on microprobe data) (Fig. 3 (e)). Biotite ($\sim$ 20 vol%) is the primary magnesium biotite (Figs. 5 (a3), 5 (b3), 5 (c3), and 5 (d3)). Quartz ($\sim$ 3 vol%), orthoclase ($\sim$ 5 vol%), and opaque minerals ($\sim$ 2 vol%) complete the mineral composition.

4.1.5 Syenite

Syenites exhibit coarse-grained anhedral to subhedral granular texture and trachytoid (Fig. 2 (f)). Orthoclase ($\sim$ 80 vol%), often showing perthitization. Fe-Mg minerals include green and brown hornblende ($4-8$ vol%), clinopyroxene (salite) ($\sim$ 4 vol%), and biotite ($\sim$ 2 vol%). Plagioclase ($\sim$ 6 vol%), quartz ($\sim$ 3 vol%), and accessory minerals such as zircon, magnetite, apatite, and rutile (up to 1 vol%) are present.

4.1.6 Monzonite

Monzonite textures range from medium- to relatively coarse-grained subhedral granular (Fig. 2 (g)) to porphyritic in some samples. Some samples contain micro-monzonitic enclaves. Alkali-feldspars and plagioclase each comprise $\sim$ 35 vol% of the rock. Based on microprobe data the chemical composition of alkali-feldspars is perthitic orthoclase ($Or_{30}Ab_{67}$) (Fig. 3 (f)). In porphyritic monzonites, plagioclases have normal zoning and their composition from the core toward the rim is labradorite to andesine (An_{50-57}) (Fig. 3 (f)). Green hornblende ($\sim$ 14 vol%), clinopyroxene (augite) (Figs. 4 (a) and 4 (f)) ($\sim$ 5 vol%), and biotite ($\sim$ 8 vol%) are present, with rare quartz, zircon, magnetite, and

Table 3. Representative electron microprobe analysis of feldspars (in wt.%) from the Nusha intrusives and the calculated structural formula (in apfu) based on 8 oxygens.

Samples	15	16	17	18	19	20	21	22	23	24
SiO_2	59.10	54.27	58.15	63.40	63.67	57.71	56.73	46.88	46.36	51.32
TiO_2	0.05	0.11	0.06	0.13	0.13	0.09	0.10	0.02	0.02	0.01
Al_2O_3	25.10	28.23	25.69	19.38	19.24	25.71	26.22	33.18	33.37	30.21
Cr_2O_3	0.00	0.01	0.01	0.01	0.02	0.02	0.00	0.00	0.01	0.00
FeOt	0.36	0.39	0.43	0.18	0.19	0.39	0.47	0.65	0.71	0.60
MnO	0.00	0.00	0.00	0.00	0.01	0.00	0.00	0.00	0.01	0.00
MgO	0.02	0.02	0.02	0.00	0.01	0.02	0.04	0.00	0.00	0.03
CaO	7.04	10.84	7.85	1.05	0.93	8.03	8.62	16.77	16.92	13.08
Na_2O	6.97	5.10	6.63	3.39	3.19	6.59	6.21	1.71	1.69	3.74
K_2O	0.80	0.34	0.64	10.42	10.75	0.50	0.50	0.08	0.07	0.23
P_2O_5	0.02	0.01	0.05	0.03	0.04	0.02	0.01	0.00	0.00	0.01
NiO	0.01	0.00	0.00	0.01	0.00	0.00	0.01	0.00	0.00	0.00
F	0.00	0.00	0.03	0.00	0.07	0.06	0.00	0.00	0.08	0.04
O=F	0.00	0.00	-0.01	0.00	-0.03	-0.03	0.00	0.00	-0.03	-0.02
Total	99.47	99.33	99.54	98.00	98.21	99.12	98.91	99.30	99.21	99.26
Si	2.65	2.47	2.62	2.93	2.95	2.61	2.57	2.17	2.15	2.35
Ti	0.002	0.004	0.002	0.005	0.005	0.003	0.004	0.001	0.001	0.000
Al	1.33	1.51	1.36	1.05	1.05	1.37	1.40	1.812	1.829	1.634
Fe^{3+}	0.000	0.000	0.000	0.000	0.000	0.000	0.000	0.000	0.000	0.000
Mn	0.000	0.000	0.000	0.000	0.001	0.000	0.000	0.000	0.001	0.000
Mg	0.001	0.001	0.001	0.000	0.001	0.001	0.003	0.000	0.000	0.002
Ca	0.339	0.529	0.379	0.052	0.046	0.390	0.420	0.833	0.843	0.643
Na	0.608	0.450	0.579	0.305	0.287	0.578	0.547	0.154	0.152	0.333
K	0.046	0.020	0.037	0.616	0.635	0.029	0.029	0.005	0.004	0.014
An	34.2	52.9	38.1	5.4	4.8	39.1	42.1	84.0	84.3	65.0
Ab	61.2	45.1	58.2	31.3	29.6	58.0	54.9	15.5	15.2	33.6
Or	4.6	2.0	3.7	63.3	65.6	2.9	2.9	0.5	0.4	1.4
Samples	25	26	27	28	29	30	31	32	33	34
SiO_2	50.71	57.33	58.67	52.63	52.24	44.70	45.05	53.27	53.71	54.66
TiO_2	0.03	0.07	0.07	0.05	0.03	0.05	0.01	0.03	0.03	0.02
Al_2O_3	30.52	26.09	24.92	29.06	29.77	35.16	34.94	29.17	29.02	27.82
Cr_2O_3	0.00	0.02	0.00	0.00	0.00	0.00	0.00	0.00	0.01	0.00
FeOt	0.64	0.63	0.64	0.65	0.52	0.50	0.50	0.55	0.53	0.49
MnO	0.00	0.00	0.00	0.00	0.02	0.00	0.00	0.01	0.00	0.03
MgO	0.03	0.03	0.01	0.07	0.03	0.00	0.00	0.05	0.04	0.04
CaO	13.55	8.18	7.14	11.88	12.62	18.31	18.33	11.69	11.52	10.18
Na_2O	3.58	6.45	7.12	4.49	3.91	0.88	0.99	4.70	4.74	5.45
K_2O	0.23	0.49	0.52	0.31	0.28	0.05	0.05	0.22	0.25	0.37
P_2O_5	0.03	0.01	0.04	0.03	0.00	0.02	0.00	0.01	0.01	0.05
NiO	0.00	0.01	0.00	0.00	0.01	0.00	0.01	0.00	0.00	0.01
F	0.00	0.00	0.00	0.00	0.00	0.00	0.00	0.00	0.00	0.00
O=F	0.00	0.00	0.00	0.00	0.00	0.00	0.00	0.00	0.00	0.00
Total	99.31	99.31	99.14	99.17	99.43	99.68	99.88	99.72	99.86	99.11
Si	2.32	2.59	2.65	2.41	2.38	2.07	2.08	2.42	2.43	2.49
Ti	0.001	0.002	0.002	0.002	0.001	0.002	0.000	0.001	0.001	0.001
Al	1.652	1.391	1.327	1.56	1.60	1.92	1.90	1.56	1.55	1.49
Fe^{3+}	0.000	0.000	0.000	0.000	0.000	0.000	0.000	0.000	0.000	0.000
Mn	0.000	0.000	0.000	0.000	0.001	0.000	0.000	0.001	0.000	0.001
Mg	0.002	0.002	0.001	0.005	0.002	0.000	0.000	0.004	0.003	0.003
Ca	0.667	0.397	0.345	0.583	0.617	0.909	0.909	0.569	0.560	0.497
Na	0.319	0.565	0.624	0.399	0.346	0.079	0.089	0.415	0.417	0.481
K	0.013	0.029	0.030	0.018	0.017	0.003	0.003	0.013	0.015	0.021
An	66.7	40.0	34.6	58.3	63.0	91.7	90.8	57.1	56.5	49.7
Ab	31.9	57.1	62.4	39.9	35.3	8.0	8.9	41.6	42.1	48.2
Or	1.3	2.8	3.0	1.8	1.7	0.3	0.3	1.3	1.5	2.1

Continued of Table 3.

Samples	35	36	37	38	39	40	41	42	43	44
SiO_2	55.53	59.87	60.13	54.06	54.50	57.84	58.42	45.73	44.95	46.07
TiO_2	0.01	0.00	0.01	0.05	0.05	0.03	0.09	0.02	0.00	0.03
Al_2O_3	27.92	17.38	18.06	28.57	28.11	25.91	25.85	34.05	34.85	34.04
Cr_2O_3	0.00	0.00	0.01	0.01	0.00	0.01	0.00	0.00	0.01	0.02
FeOt	0.58	0.08	0.07	0.56	0.69	0.44	0.60	0.52	0.50	0.53
MnO	0.03	0.02	0.04	0.01	0.01	0.01	0.01	0.02	0.00	0.01
MgO	0.05	0.00	0.01	0.04	0.09	0.03	0.02	0.06	0.05	0.07
CaO	10.19	8.85	8.98	11.00	10.37	7.52	7.55	17.61	18.18	17.52
Na_2O	5.38	0.37	0.47	5.00	5.26	6.67	6.65	1.23	0.94	1.39
K_2O	0.38	0.11	0.11	0.31	0.35	0.86	0.84	0.04	0.02	0.04
P_2O_5	0.01	0.00	0.01	0.04	0.05	0.02	0.02	0.00	0.00	0.00
NiO	0.00	0.01	0.00	0.01	0.02	0.00	0.01	0.00	0.01	0.00
F	0.00	0.00	0.00	0.01	0.05	0.00	0.00	0.13	0.00	0.10
O=F	0.00	0.00	0.00	-0.01	-0.02	0.00	0.00	-0.05	0.00	-0.04
Total	100.09	86.68	87.90	99.65	99.52	99.34	100.05	99.35	99.53	99.78
Si	2.50	2.98	2.96	2.45	2.47	2.61	2.62	2.12	2.08	2.13
Ti	0.000	0.000	0.001	0.002	0.002	0.001	0.003	0.001	0.000	0.001
Al	1.48	1.02	1.04	1.52	1.50	1.38	1.36	1.86	1.90	1.85
Fe^{+3}	0.000	0.000	0.000	0.000	0.000	0.000	0.000	0.000	0.000	0.000
Mn	0.001	0.001	0.002	0.000	0.001	0.000	0.000	0.001	0.000	0.000
Mg	0.004	0.000	0.001	0.003	0.006	0.002	0.001	0.004	0.003	0.005
Ca	0.492	0.473	0.473	0.535	0.505	0.364	0.363	0.877	0.904	0.869
Na	0.470	0.036	0.045	0.440	0.464	0.584	0.578	0.111	0.085	0.125
K	0.022	0.007	0.007	0.018	0.020	0.049	0.048	0.002	0.001	0.002
An	50.0	91.7	90.1	53.9	51.1	36.5	36.7	88.6	91.3	87.2
Ab	47.8	6.9	8.6	44.3	46.9	58.6	58.5	11.2	8.5	12.5
Or	2.2	1.4	1.3	1.8	2.0	5.0	4.9	0.2	0.1	0.2

Samples	45	46	47	48	49	50	51	52	53	54
SiO_2	45.62	46.51	48.99	44.40	44.77	55.92	56.54	55.18	55.12	55.51
TiO_2	0.01	0.06	0.07	0.00	0.02	0.08	0.11	0.10	0.17	0.09
Al_2O_3	34.22	33.27	31.53	34.88	34.87	27.10	26.62	27.34	27.14	27.25
Cr_2O_3	0.00	0.00	0.00	0.00	0.00	0.00	0.00	0.00	0.00	0.00
FeOt	0.49	0.62	0.83	0.53	0.50	0.65	0.69	0.60	0.64	0.54
MnO	0.00	0.00	0.00	0.00	0.01	0.00	0.01	0.00	0.01	0.00
MgO	0.07	0.09	0.23	0.05	0.09	0.07	0.07	0.09	0.10	0.07
CaO	17.83	16.95	14.97	18.26	18.12	9.53	9.56	10.26	10.20	9.83
Na_2O	1.22	1.70	2.78	1.03	1.09	5.69	5.61	5.22	5.27	5.65
K_2O	0.04	0.06	0.14	0.02	0.04	0.54	0.54	0.48	0.50	0.51
P_2O_5	0.00	0.01	0.00	0.00	0.00	0.03	0.03	0.04	0.01	0.00
NiO	0.00	0.01	0.00	0.00	0.00	0.01	0.00	0.00	0.00	0.00
F	0.00	0.00	0.01	0.04	0.04	0.11	0.11	0.00	0.04	0.00
O=F	0.00	0.00	0.00	-0.02	-0.02	-0.05	-0.05	0.00	-0.02	0.00
Total	99.51	99.28	99.54	99.20	99.54	99.69	99.84	99.32	99.20	99.45
Si	2.11	2.15	2.25	2.07	2.08	2.53	2.55	2.50	2.51	2.52
Ti	0.000	0.002	0.002	0.000	0.001	0.003	0.004	0.003	0.006	0.003
Al	1.86	1.81	1.71	1.91	1.90	1.44	1.41	1.46	1.45	1.45
Fe^{3+}	0.000	0.000	0.000	0.000	0.000	0.000	0.000	0.000	0.000	0.000
Mn	0.000	0.000	0.000	0.000	0.001	0.000	0.000	0.000	0.000	0.000
Mg	0.005	0.006	0.016	0.004	0.006	0.005	0.004	0.006	0.007	0.004
Ca	0.886	0.842	0.739	0.913	0.902	0.463	0.463	0.500	0.498	0.478
Na	0.110	0.153	0.248	0.093	0.098	0.500	0.492	0.460	0.466	0.497
K	0.002	0.004	0.008	0.001	0.002	0.031	0.031	0.028	0.029	0.030
An	88.8	84.3	74.2	90.6	89.9	46.6	47.0	50.6	50.2	47.6
Ab	11.0	15.3	24.9	9.2	9.8	50.3	49.9	46.6	46.9	49.5
Or	0.2	0.3	0.8	0.1	0.2	3.1	3.2	2.8	2.9	2.9

Continued of Table 3.

Samples	55	56	57	58	59	60	61	62	63
SiO_2	55.99	65.76	65.82	54.82	54.85	58.77	58.04	59.24	59.42
TiO_2	0.10	0.04	0.07	0.04	0.03	0.00	0.01	0.00	0.03
Al_2O_3	27.06	19.80	20.08	28.30	28.42	25.71	26.25	25.40	24.83
Cr_2O_3	0.00	0.01	0.00	0.01	0.01	0.00	0.00	0.00	0.01
FeOt	0.54	0.24	0.29	0.26	0.24	0.18	0.21	0.25	0.26
MnO	0.00	0.00	0.00	0.00	0.02	0.01	0.00	0.01	0.01
MgO	0.08	0.00	0.02	0.00	0.00	0.00	0.00	0.00	0.03
CaO	9.65	1.02	1.20	10.49	10.55	7.49	7.95	7.24	6.70
Na_2O	5.69	7.04	7.76	5.38	5.29	6.82	6.71	7.06	6.67
K_2O	0.50	5.80	4.86	0.26	0.28	0.46	0.44	0.52	1.10
P_2O_5	0.02	0.01	0.01	0.01	0.03	0.00	0.04	0.00	0.01
NiO	0.02	0.02	0.00	0.00	0.01	0.00	0.01	0.00	0.00
F	0.03	0.00	0.00	0.05	0.00	0.00	0.03	0.00	0.04
O=F	-0.01	0.00	0.00	-0.02	0.00	0.00	-0.01	0.00	-0.02
Total	99.67	99.73	100.11	99.60	99.72	99.45	99.68	99.73	99.09
Si	2.53	2.94	2.93	2.48	2.48	2.64	2.60	2.65	2.68
Ti	0.003	0.001	0.002	0.001	0.001	0.000	0.000	0.000	0.001
Al	1.44	1.04	1.05	1.51	1.51	1.36	1.39	1.34	1.32
Fe^{+3}	0.000	0.000	0.000	0.000	0.000	0.000	0.000	0.000	0.000
Mn	0.000	0.000	0.000	0.000	0.001	0.001	0.000	0.001	0.000
Mg	0.005	0.000	0.001	0.000	0.000	0.000	0.000	0.000	0.002
Ca	0.468	0.049	0.057	0.509	0.511	0.361	0.383	0.347	0.324
Na	0.500	0.612	0.670	0.473	0.464	0.594	0.585	0.613	0.583
K	0.029	0.332	0.277	0.015	0.016	0.026	0.025	0.030	0.063
An	47.0	4.9	5.7	51.1	51.6	36.7	38.6	35.1	33.4
Ab	50.1	61.6	66.8	47.4	46.8	60.6	58.9	61.9	60.1
Or	2.9	33.4	27.5	1.5	1.6	2.7	2.5	3.0	6.5

apatite (up to 3 vol%).

4.1.7 Monzodiorite

Monzodiorite typically exhibit fine to medium-grained anhedral granular textures (Fig. 2 (h)). Plagioclase ($\sim$ 60 vol%) is the dominant mineral, showing normal zoning (An_{38-51}) in fine-grained ones (Fig. 3 (g)). Alkali-feldspars ($\sim$ 20 vol%) is microperthitic orthoclase ($Or_{35}Ab_{63}$) (Fig. 3 (g)), while clinopyroxene ($\sim$ 10 vol%) is augite (Figs. 4 (a) and 4 (g)). Biotite ($\sim$ 7 vol%) is primary Mg-biotite (Figs. 5 (a4), 5 (b4), 5 (c4), and 5 (d4)). Quartz ($\sim$ 3 vol%) is also present.

4.1.8 Granodiorite

Granodiorites display porphyritic textures with large plagioclase and green hornblende crystals in a relatively fine-grained groundmass of quartz, plagioclase, green hornblende, orthoclase, and opaque minerals (Fig. 2 (i)). Plagioclase ($\sim$ 63 vol%) exhibits normal zoning and oligoclase composition (based on the extinction angle), and orthoclase ($\sim$ 8 vol%) shows perthitization. Quartz ($\sim$ 20 vol%) fills interstitial spaces, while hornblende brown hornblende ($\sim$ 7 vol%), and opaque minerals ($\sim$ 2 vol%), are also present.

4.1.9 Quartz monzonite

Quartz monzonites exhibit medium- to relatively coarse-grained anhedral granular textures (Fig. 2 (j)). Various textures, porphyritic with relatively fine-grained groundmass, monzonitic, rapakivi, micrographic, and myrmekitic textures are observed. Orthoclase and plagioclase each constitute $30-40$ vol% of the rock, quartz $7-15$ vol%, biotite up to vol%, hornblende (brown and green) up to 10 vol%, clinopyroxene (augite) up to 5 vol%, with accessory minerals such as opaque minerals, zircon, apatite, and sphene (up to 1 vol%). Dioritic and micro-monzonitic enclaves are rarely present.

4.2 Whole-rock geochemistry

The major oxides contents in Nusha intrusive rocks are as follow (Table 1): SiO_2 ($45.31-70.05$ wt%), Al_2O_3 ($14.62-19.28$ wt%), K_2O ($7.29-0.98$ wt%), Na_2O ($1.3-5.04$ wt%), CaO ($12.19-1.74$ wt%), MgO ($10.33-0.51$ wt%), FeOt ($12.84-2.46$ wt%), TiO_2 ($1.99-0.28$ wt%), and P_2O_5 ($0.66-0.06$ wt%). Discrimination diagrams for K_2O vs. SiO_2 (Peccerillo and Taylor, 1976) and Ce/Yb vs. Ta/Yb (Pearce, 1982) classify the Nusha intrusive rocks as high-K calc-alkaline to shoshonitic, consistent with the

Table 4. Representative electron microprobe analysis of pyroxenes (in wt.%) from the Nusha intrusives and the calculated structural formula (in apfu) and end members (in mole%) based on 6 oxygens.

Samples	70	71	72	73	74	75	76	77	78	79
SiO_2	50.53	50.33	52.18	51.95	51.76	51.54	52.04	51.46	51.09	51.06
TiO_2	0.96	0.98	0.45	0.35	0.45	0.53	0.65	0.72	0.61	0.59
Al_2O_3	2.05	2.17	2.08	1.82	1.94	2.71	1.24	1.76	3.12	3.30
Cr_2O_3	0.01	0.00	0.21	0.03	0.03	0.06	0.00	0.01	0.03	0.02
FeOt	11.20	10.98	8.32	8.38	9.00	8.83	12.58	12.42	8.38	8.58
MnO	0.35	0.33	0.27	0.25	0.29	0.22	0.43	0.38	0.19	0.22
MgO	14.86	15.04	15.08	15.51	14.83	14.88	15.18	15.01	15.94	15.61
CaO	19.26	19.41	21.49	21.36	21.52	21.35	18.32	18.43	20.86	20.56
Na_2O	0.27	0.28	0.44	0.34	0.35	0.38	0.28	0.32	0.22	0.27
K_2O	0.00	0.00	0.00	0.00	0.00	0.01	0.02	0.00	0.00	0.00
P_2O_5	0.01	0.01	0.07	0.02	0.00	0.00	0.03	0.03	0.02	0.00
NiO	0.00	0.00	0.00	0.01	0.00	0.03	0.01	0.01	0.00	0.00
F	0.13	0.04	0.02	0.20	0.00	0.00	0.00	0.01	0.01	0.06
O=F	-0.06	-0.01	-0.01	-0.08	0.00	0.00	0.00	0.00	-0.01	-0.03
Total	99.59	99.55	100.61	100.14	100.19	100.54	100.79	100.56	100.46	100.24
Si	1.911	1.901	1.930	1.936	1.930	1.912	1.942	1.926	1.891	1.895
Ti	0.027	0.028	0.013	0.010	0.013	0.015	0.018	0.020	0.017	0.017
AlIV	0.078	0.084	0.067	0.071	0.071	0.086	0.049	0.066	0.108	0.103
AlVI	0.013	0.011	0.023	0.008	0.014	0.031	0.005	0.011	0.027	0.040
Fe^{3+}	0.084	0.93	0.069	0.086	0.081	0.081	0.065	0.077	0.095	0.081
Fe^{2+}	0.267	0.25	0.187	0.172	0.197	0.191	0.326	0.309	0.162	0.183
Mn	0.011	0.011	0.008	0.008	0.009	0.007	0.014	0.012	0.006	0.007
Mg	0.838	0.847	0.832	0.862	0.824	0.823	0.845	0.837	0.879	0.863
Ca	0.708	0.785	0.852	0.853	0.860	0.849	0.733	0.739	0.827	0.817
Na	0.020	0.020	0.031	0.025	0.026	0.028	0.020	0.023	0.016	0.019
K	0.000	0.000	0.000	0.000	0.000	0.000	0.001	0.000	0.000	0.000
Wo	39.34	39.47	43.69	42.99	43.55	43.46	36.93	37.37	41.94	41.83
En	42.23	42.56	42.66	43.44	41.76	42.15	42.58	42.35	44.59	44.19
Fs	18.42	17.96	13.63	13.56	14.68	14.38	20.48	20.27	13.45	13.98
Mg#	0.75	0.77	0.81	0.83	0.80	0.81	0.72	0.72	0.84	0.82
Samples	80	81	82	83	84	85	86	87	88	89
SiO_2	52.76	52.28	50.53	51.64	52.19	50.36	50.09	51.11	49.67	50.87
TiO_2	0.36	0.35	1.01	0.44	0.36	1.17	1.16	0.99	0.96	0.60
Al_2O_3	0.63	0.64	2.51	2.78	2.50	3.15	3.01	2.50	4.18	3.15
Cr_2O_3	0.02	0.00	0.01	0.03	0.00	0.01	0.01	0.01	0.01	0.00
FeOt	23.44	23.62	12.24	8.30	8.03	8.61	8.31	8.25	8.16	8.25
MnO	0.63	0.68	0.39	0.23	0.23	0.24	0.20	0.27	0.20	0.30
MgO	21.81	21.82	14.49	15.73	15.92	14.90	14.70	15.04	14.05	14.78
CaO	1.88	1.94	18.61	21.19	21.28	21.36	21.79	21.36	22.06	22.02
Na_2O	0.00	0.00	0.34	0.20	0.19	0.47	0.52	0.56	0.64	0.30
K_2O	0.00	0.00	0.01	0.00	0.00	0.00	0.01	0.01	0.00	0.00
P_2O_5	0.00	0.01	0.01	0.03	0.02	0.04	0.03	0.04	0.01	0.01
NiO	0.00	0.01	0.02	0.03	0.00	0.01	0.02	0.00	0.00	0.00
F	0.07	0.05	0.17	0.11	0.00	0.06	0.00	0.14	0.00	0.00
O=F	-0.03	-0.02	-0.07	-0.05	0.00	-0.03	0.00	-0.06	0.00	0.00
Total	101.56	101.39	100.29	100.66	100.73	100.34	99.84	100.23	99.94	100.27
Si	1.957	1.947	1.904	1.909	1.921	1.877	1.876	1.905	1.858	1.89
Ti	0.010	0.010	0.029	0.012	0.010	0.033	0.033	0.028	0.027	0.017
AlIV	0.044	0.058	0.083	0.092	0.079	0.109	0.111	0.086	0.136	0.106
AlVI	-0.017	-0.030	0.027	0.028	0.029	0.028	0.020	0.023	0.046	0.031
Fe^{+3}	0.06	0.88	0.081	0.077	0.063	0.114	0.128	0.103	0.136	0.097
Fe^{+2}	0.663	0.642	0.302	0.178	0.183	0.152	0.129	0.152	0.117	0.158
Mn	0.020	0.022	0.013	0.007	0.007	0.008	0.006	0.009	0.007	0.009
Mg	1.206	1.211	0.814	0.867	0.873	0.828	0.821	0.835	0.783	0.819
Ca	0.075	0.078	0.751	0.839	0.839	0.853	0.874	0.853	0.884	0.878
Na	0.000	0.000	0.025	0.015	0.014	0.034	0.037	0.041	0.047	0.021
K	0.000	0.000	0.001	0.000	0.000	0.000	0.001	0.000	0.000	0.000
Wo	3.68	3.78	38.26	42.60	42.66	43.59	44.57	43.64	45.82	44.70
En	59.47	59.21	41.45	44.00	44.40	42.30	41.83	42.76	40.61	41.74
Fs	36.83	37.00	20.27	13.39	12.93	14.10	13.59	13.59	13.56	13.55
Mg#	0.64	0.65	0.72	0.82	0.82	0.84	0.86	0.84	0.86	0.83

Continued of Table 4.

Samples	90	91	92	93	94	95	96
SiO_2	50.59	51.48	52.21	49.54	50.94	49.74	51.12
TiO_2	0.58	0.56	0.44	1.29	0.99	1.11	0.90
Al_2O_3	3.08	2.22	1.64	3.83	2.22	3.53	2.22
Cr_2O_3	0.00	0.04	0.02	0.02	0.00	0.05	0.00
FeOt	8.63	9.33	9.15	10.13	9.74	9.68	10.35
MnO	0.32	0.43	0.37	0.24	0.27	0.25	0.29
MgO	15.20	15.15	15.61	14.63	15.60	14.81	16.13
CaO	21.26	20.44	20.69	20.10	19.97	20.44	18.73
Na_2O	0.28	0.42	0.41	0.33	0.33	0.32	0.23
K_2O	0.01	0.00	0.00	0.01	0.01	0.00	0.01
P_2O_5	0.03	0.02	0.02	0.02	0.02	0.01	0.00
NiO	0.00	0.01	0.01	0.00	0.00	0.02	0.01
F	0.00	0.15	0.00	0.00	0.00	0.00	0.15
O=F	0.00	-0.07	0.00	0.00	0.00	0.00	-0.06
Total	99.99	100.18	100.58	100.12	100.10	99.95	100.07
Si	1.888	1.923	1.935	1.856	1.902	1.865	1.911
Ti	0.016	0.016	0.012	0.036	0.028	0.031	0.025
AlIV	0.113	0.078	0.066	0.124	0.085	0.121	0.080
AlVI	0.022	0.019	0.005	0.043	0.012	0.033	0.017
Fe^{+3}	0.11	0.08	0.08	0.08	0.10	0.11	0.07
Fe^{+2}	0.12	0.14	0.14	0.17	0.16	0.15	0.23
Mn	0.010	0.014	0.012	0.008	0.009	0.008	0.009
Mg	0.846	0.844	0.862	0.817	0.868	0.827	0.898
Ca	0.850	0.818	0.822	0.807	0.799	0.821	0.750
Na	0.021	0.031	0.029	0.024	0.024	0.023	0.017
K	0.000	0.000	0.000	0.000	0.000	0.000	0.000
Wo	43.03	41.59	41.50	40.35	41.39	41.88	37.85
En	42.81	42.89	43.57	43.85	41.92	42.22	45.35
Fs	14.14	15.51	14.91	15.79	16.67	15.88	16.79
Mg#	0.84	0.80	0.81	0.80	0.79	0.81	0.78

mineral chemistry (Figs. 6 (a) & 6 (b)).

The REE patterns for the Nusha intrusive rocks, normalized to primitive mantle values (McDonough et al., 1992) (Fig. 6 (c)), show similar patterns across the samples, indicating a common origin. These patterns show REE enrichment with little or no Eu anomaly ($Eu/Eu^* = 0.66 - 1.62$, mean $= 1.05$). High differentiation of HREE from LREE ($La_N/Lu_N = 12.93 - 3.46$, Mean $= 7.52$), with low differentiation of LREE from MREE ($Gd_N/Lu_N = 1.83 - 0.84$, Mean $= 1.25$), resulting in a negative LREE slope and a flat HREE slope (Fig. 6 (c)).

Spider diagrams normalized to the primitive mantle (Taylor and McLennan, 1985) (Fig. 6 (d)), reveal enrichment of all elements (except for Ti and Zr). Moreover, Ba, Ta, Zr, Sr, Ti, Nb, Hf, U and Y show negative anomalies, while Rb, Th, K, Nd, Tb, Pb, La, and Sm display positive anomalies.

5. Discussion

5.1 Chemistry of minerals

5.1.1 Magmatic series and tectonomagmatic setting

The chemical composition of certain minerals reflects the environment and the parent magma from which they were formed, making it possible to infer the characteristics of the parental magma through the chemical composition of these minerals (Le Bas, 1962). Clinopyroxenes, with their wide range of chemical compositions, are particularly useful in understanding the origin, nature, and tectonomagmatic setting of the magmas that formed these minerals (Leterrier et al., 1982; Ovung et al., 2018; Liang et al., 2018). According to Le Bas (1962), the concentrations of Ti, Si, and Al in pyroxenes are influenced by the degree of magma alkalinity. Microanalysis data for the clinopyroxenes in the Nusha intrusive rocks, plotted on the SiO_2-Al_2O_3 diagram (Le Bas, 1962), indicate that these rocks belong to the sub-alkaline magmatic series (Fig. 7 (a)). The F2 - F1 diagram (Leter-

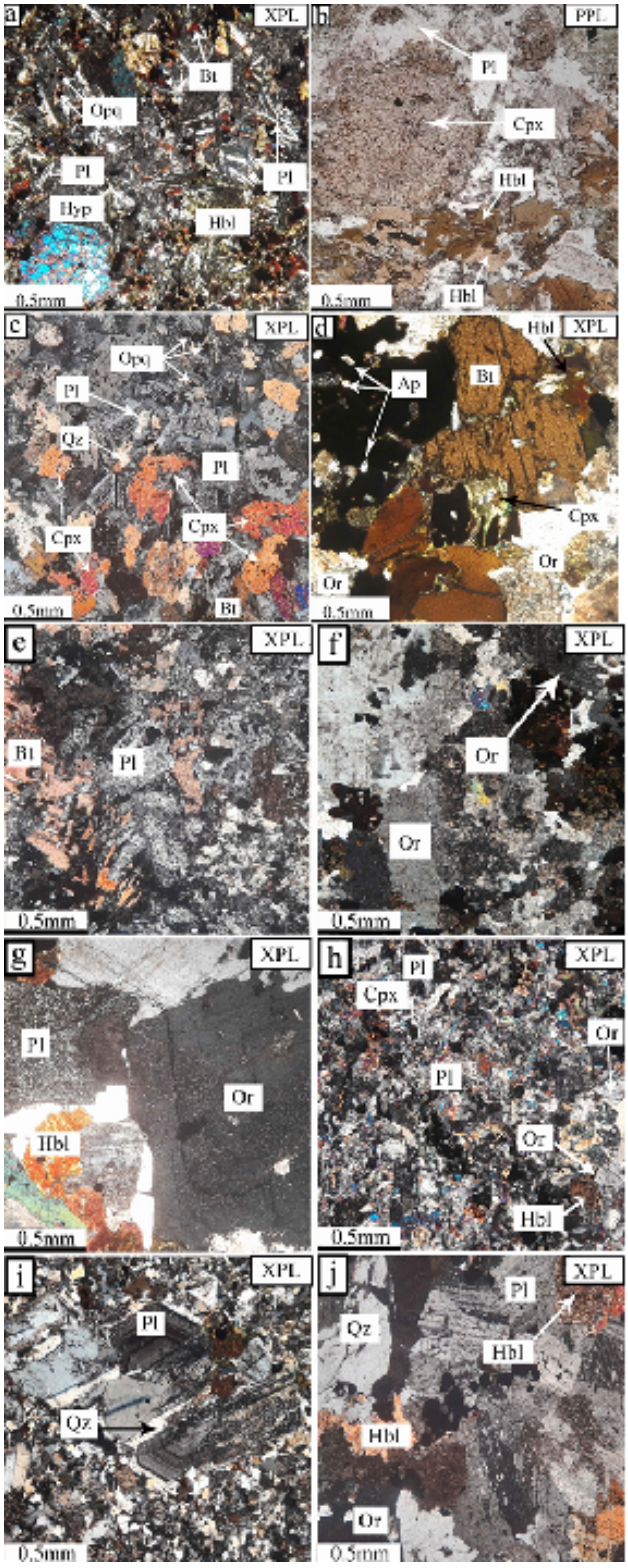

Figure 2. Microscopic images of: (a) Gabbronorite, (b) and (c) Gabbro, (d) Monzogabbro, (e) Diorite, (f) Syenite, (g) Monzonite, (h) Monzodiorite, (i) Granodiorite, and (j) Quartz monzonite from Nusha area. Abbreviations after Whitney and Evans (2010) (Pl: Plagioclase, Op: Opaque, Bt: Biotite, Hbl: Hornblende, Qz: Quartz, Cpx: Clinopyroxene, Or: Orthoclase, Ap: Apatite, Opx: Orthopyroxene).

rier et al., 1982) further discriminates the tectonomagmatic settings of the rocks based on clinopyroxene composition. The values of F2 and F1 were obtained using the following formulas.

F1 = -0.012SiO_2 - 0.0807TiO_2 + 0.0026Al_2O_3 - 0.0012FeOt - 0.0026MnO + 0.0087MgO - 0.0128CaO - 0.0419Na_2O

F2 = -0.0469SiO_2 - 0.0818TiO_2 - 0.0212Al_2O_3 - 0.0041FeOt - 0.1435MnO - 0.0029MgO + 0.085CaO + 0.0160Na_2O

The calculated F2 and F1 values, using the Leterrier et al. (1982) equations, suggest a volcanic arc setting for the Nusha intrusive rocks (Fig. 7 (b)).

Biotite is also useful in determining the geochemical characteristics, origin, and tectonomagmatic setting of their parental magma (Abdel-Rahman, 1994). Discriminant diagrams for biotite using Al_2O_3-MgO, MgO-Al_2O_3-FeO, and Al_2O_3-FeO show that the magmatic series and tectonomagmatic setting are consistent with a volcanic arc origin (Figs. 7 (b), 7 (c), 7 (d) and 7 (e)). The last diagrams indicate that these rocks belong to orogenic settings as well. Zhou (1986) $FeO^{+2}/(FeO^{+2}+MgO)$-MgO diagram confirms that the Nusha intrusive rocks are of mixed crust-mantle origin (Fig. 7 (f)).

5.1.2 Evaluation of pressure and temperature

In this section, the temperature and pressure at which the Nusha intrusive rocks formed are assessed using conventional geothermobarometric methods based on mineral composition.

5.1.3 Geothermometry and geobarometry based on clinopyroxene composition

The chemical composition of pyroxenes is a key tool for estimating temperature in igneous rocks. The XPT and YPT indices, calculated using Soesoo (1997) equations, were used to determine the formation temperatures of the clinopyroxenes. XPT and YPT were obtained based on Soesoo (1997) suggested equations.

XPT = 0 .446SiO_2 + 0.187TiO_2 -0.404Al_2O_3 + 0.346FeO - 0.052MnO + 0.309MgO + 0.446CaO - 0.446Na_2O

YPT = - 0.369SiO_2 + 0.535TiO_2 - 0.317Al_2O_3 + 0.232FeO + 0.235MnO - 0.516MgO - 0.167CaO - 0.153Na_2O

One of the significant advantages of this method in thermometry is that it does not require the presence of two pyroxenes simultaneously, and it can be used for different Mg-Ca-Fe and Fe-Mg pyroxenes. According to this method, the crystallization temperature of the clinopyroxenes in the Nusha intrusive rocks ranges from 1170 to 1210 °C (Fig. 8 (a)). The crystallization pressures were estimated to be 3 to 7 kb, predominantly in the range of 6 to 7 kb (Fig. 8 (b)).

5.1.4 Biotite thermometer

To estimate the crystallization temperatures of biotite-bearing intrusive rocks, the Henry et al. (2005) thermometer, based on the Ti-Mg/(Mg+Fe) ratio, was used. The crystallization temperatures of the biotite in the Nusha intrusive rocks range from 760 to 850 °C (Fig.9).

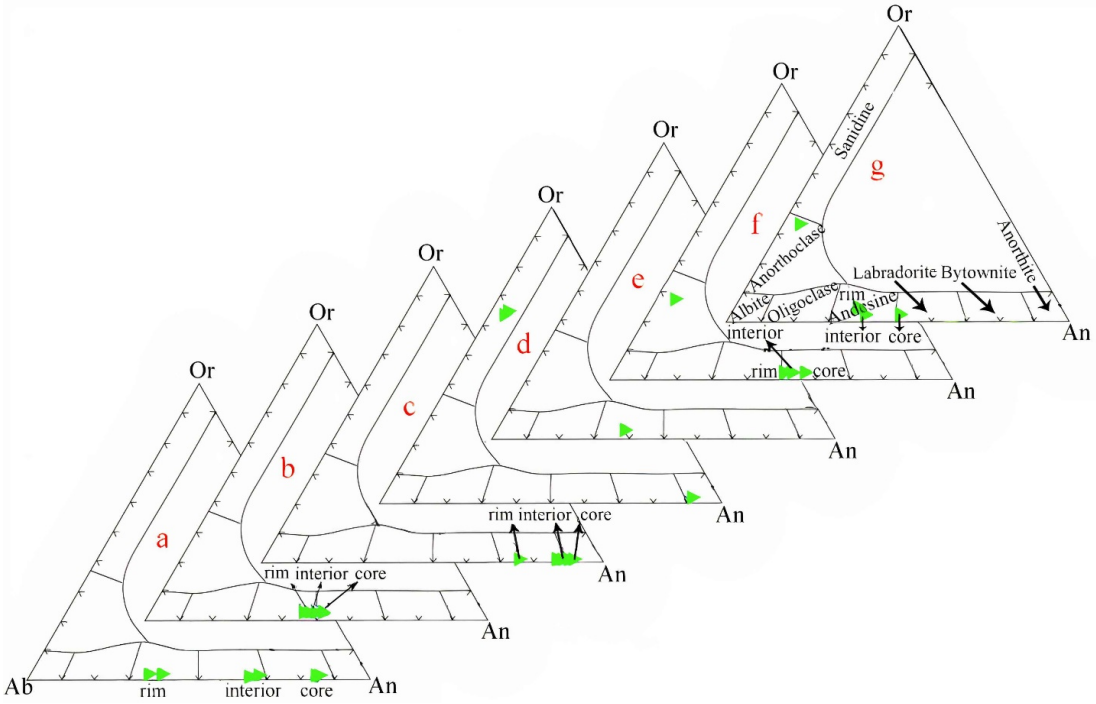

Figure 3. The chemical composition of feldspars of the Nusha area on the Ab-Or-An ternary classification diagram (Deer et al., 1991) separated by rock type, (a) gabbronorite, (b) gabbro (porphyritic), (c) gabbro (intergranular), (d) monzogabbro, (e) diorite, (f) monzonite, (g) monzodiorite.

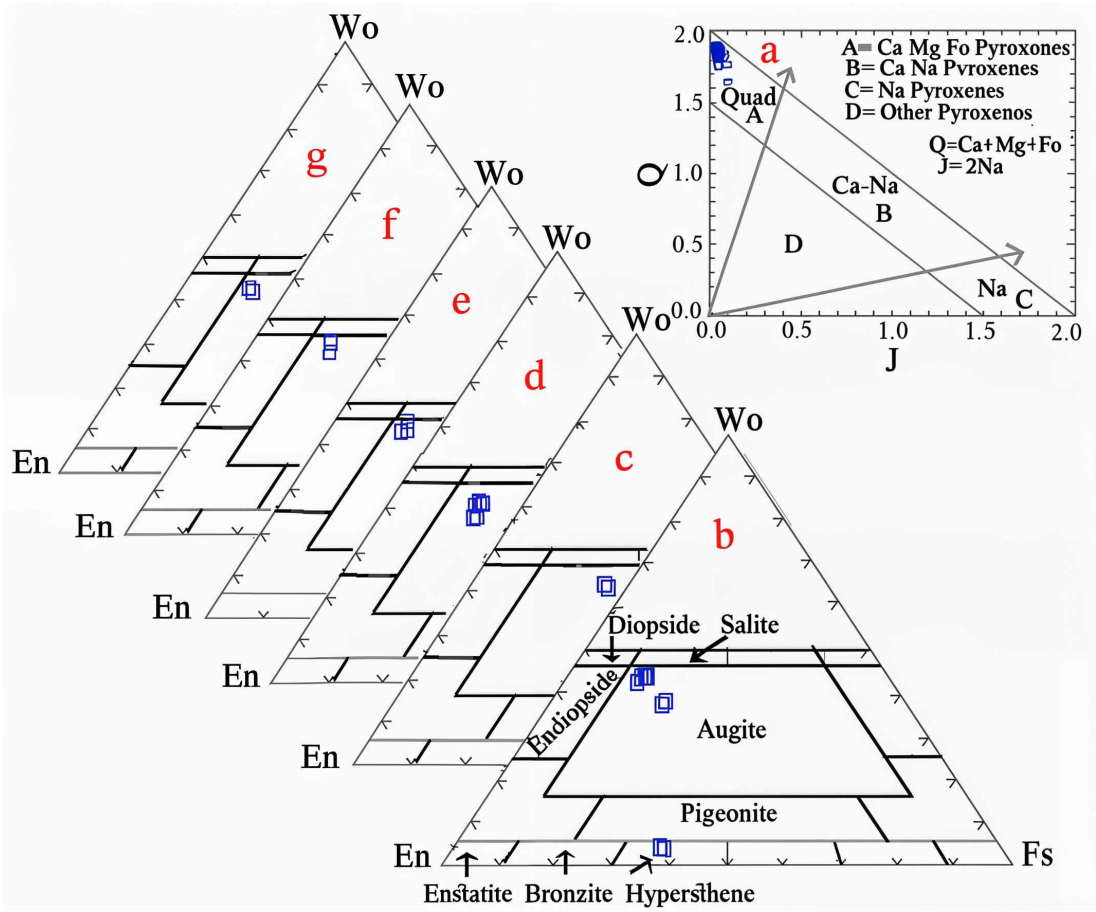

Figure 4. The chemical composition of different pyroxenes of the Nusha area on the, a-Q-J diagram (Morimoto et al., 1988) and on the Wo-En-Fs classification diagram (Poldervaart and Hess, 1968) separated by rock type, (b) gabbronorite, (c) gabbro (porphyritic), (d) gabbro (intergranular), (e) monzogabbro, (f) monzonite, (g) monzodiorite

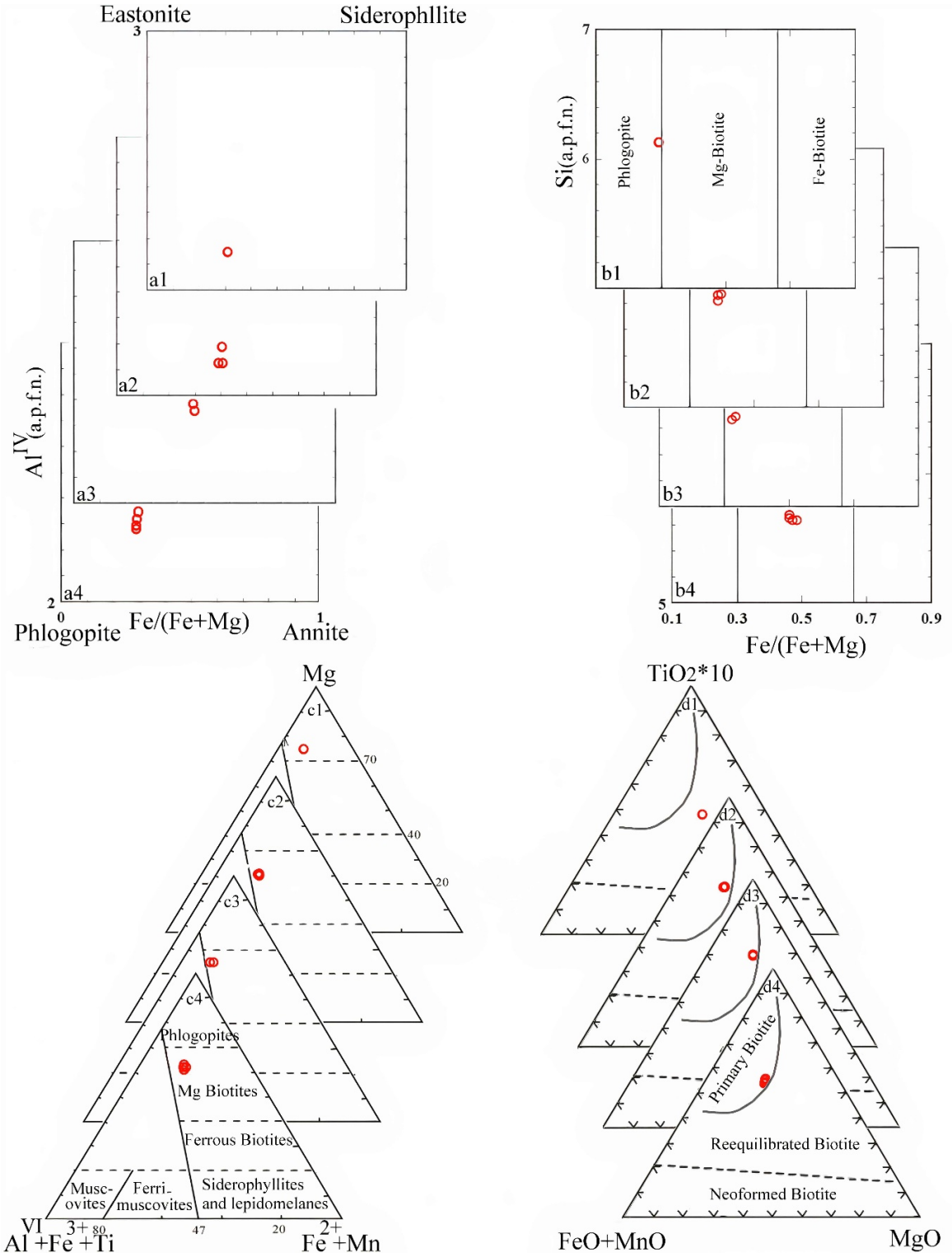

Figure 5. The chemical composition of biotites of, (1) gabbronorite, (2) monzogabbro, (3) diorite and (4) monzodiorite of the Nusha area on, (a) AlIV vs. Fe/(Fe+Mg) (Speer, 1984), (b) Si vs. Fe/(Fe+Mg) (Forster, 1960), (c) Mg-(Al^{VI}+Fe^{2+}+Ti)-(Fe^{2+}+Mn) (Forster, 1960), and (d) TiO_2-(FeO+MnO)-MgO (Nachite et al., 2005) diagrams.

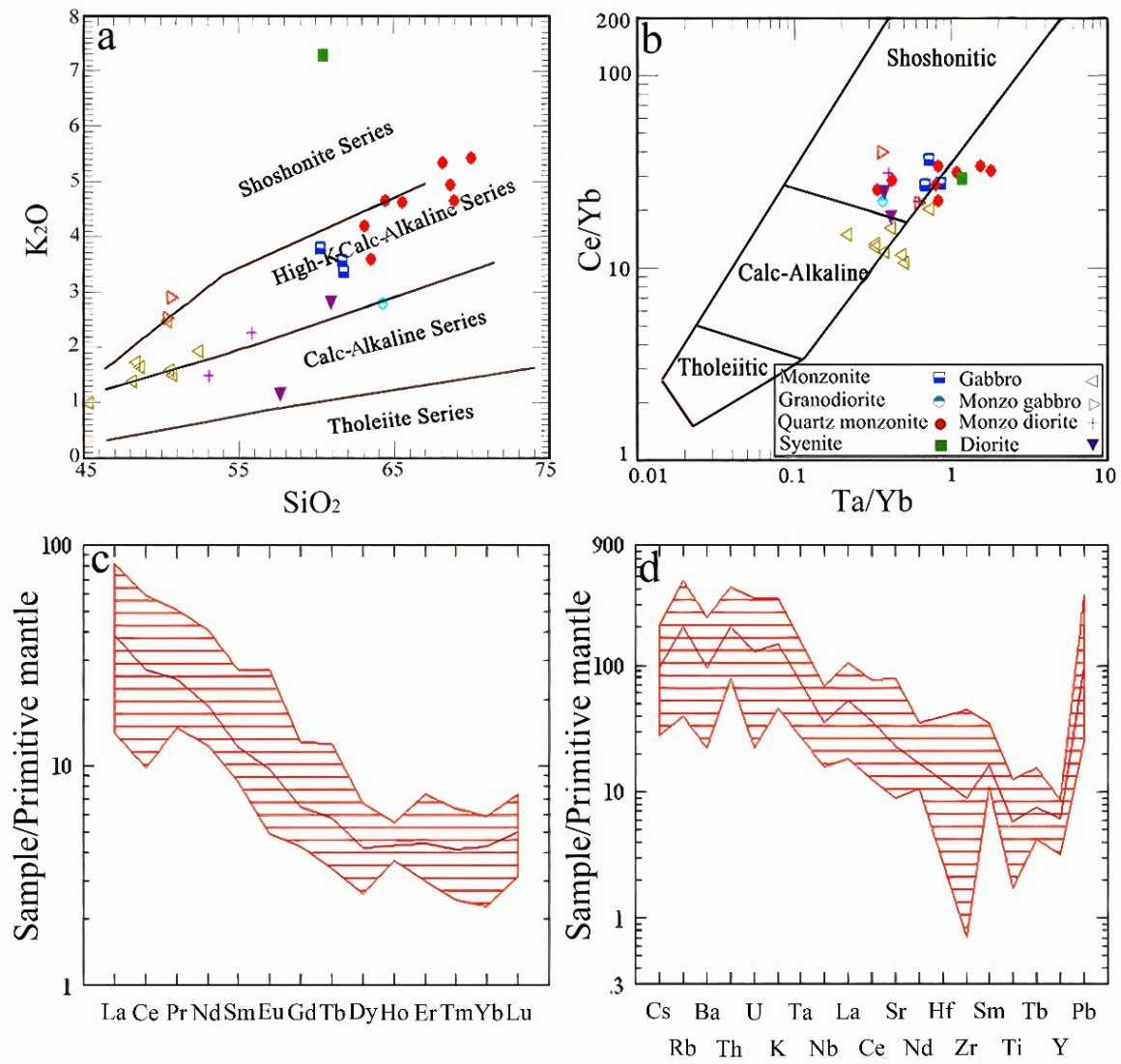

Figure 6. (a) and (b) The Nusha area intrusive samples plotted on the K_2O vs. SiO_2 (Peccerillo and Taylor, 1976) and Ce/Yb vs. Ta/Yb (Pearce, 1982) magmatic series discrimination diagrams, which indicate a high-potassium calc-alkaline and shoshonite series. (c) and (d) The whole (hatched area) and mean (middle red line) patterns of REEs normalized to primitive mantle based on McDonough et al. (1992) data, and the whole (hatched area) and mean (middle red line) multi-element spider diagrams normalized to the primitive mantle based on Taylor and McLennan (1985) data, of the Nusha area intrusives respectively.

5.2 Whole-rock chemistry

5.2.1 Tectonomagmatic setting

Geochemical data, especially immobile trace element ones, provide valuable information about the origin and tectonomagmatic setting of intrusive rocks. Several pieces of evidence suggest that the Nusha intrusive rocks were emplaced in an active setting. For example, Nb/Y ratios in subduction continental margin zones typically range from 0.32 to 1.72 (Temel et al., 1998; Pearce, 1983), and in the Nusha samples, these ratios vary between 0.38 and 1.60. The L-shaped REE patterns of the Nusha intrusive rocks are typical of calc-alkaline rocks formed in continental margins of subduction zones (Winter, 2001) (Fig. 6 (c)). Furthermore, negative Nb and Ti anomalies in spider diagrams are indicative of subduction-related magmas (Pearce, 1982), while positive anomalies are characteristic of rift-related magmas (Ballèvre et al., 2001). According to many researchers, the enrichment in LILE and LREE and the low concentration of HREE and HFSE along with the negative anomaly of Nb and Ti are signs of magmas related to the subduction zone (Gass et al., 1984; Wilson, 1989; Foley and Wheller, 1990; Pearce and Parkinson, 1993; Wang et al., 2004). Positive anomalies of K and LILEs, and negative anomalies of Nb, Zr, and Ti elements are significant characteristics of magmas related to subduction zones.

Tectonomagmatic discrimination diagrams further support a continental arc setting. The Th/Hf-Ta/Hf diagram (Schandl and Gorton, 2002) places all the Nusha samples within the volcanic arc field of an active continental margin (Fig. 10 (a)). Similarly, Th/Yb vs. Ta/Yb diagram (Pearce, 2008) confirms an active continental margin arc setting (Fig. 13 (c)). The Sr/Y, La/Yb ratios, and Y and Yb contents (Castillo, 2012; Defant and Drummond, 1990) classify the Nusha intrusions as normal arc types, distinct from adakites (Fig. 10 (b)). The tectonomagmatic results obtained from whole-rock chemistry are consistent with

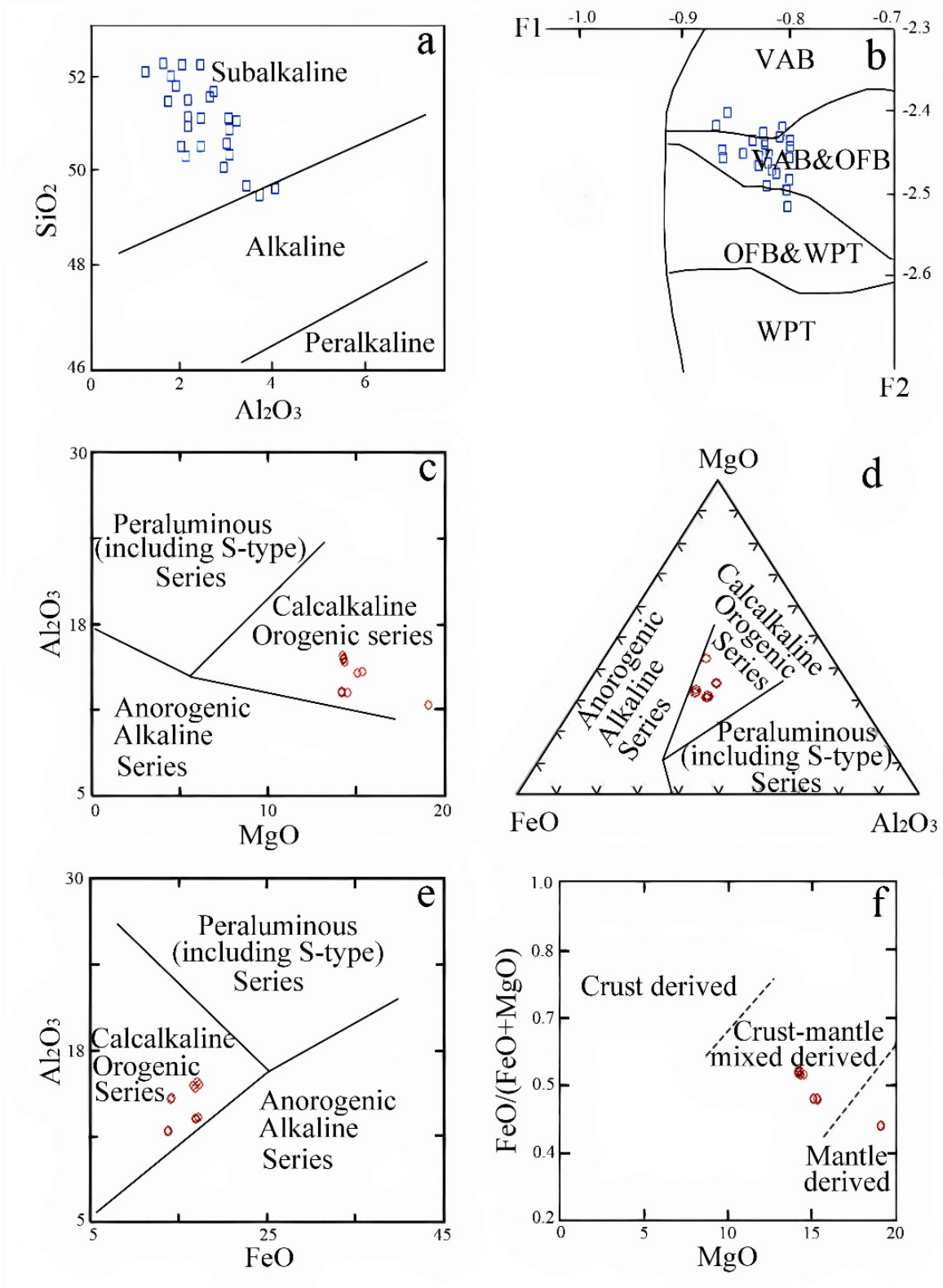

Figure 7. (a) and (b) The diagrams of SiO_2-Al_2O_3 (Le Bas, 1962) and F1-F2 (Leterrier et al., 1982) for discriminating magmatic series and tectonomagmatic setting respectively using microprobe results of clinopyroxenes, (c) to (e) The Al_2O_3-MgO, MgO-FeO-Al_2O_3, and Al_2O_3-FeO diagrams (Abdel-Rahman, 1994) for discriminating magmatic series and tectonomagmatic setting using the microprobe results of the biotite, and (f) The $FeO^{+2}/(FeO^{+2}+MgO)$-MgO diagram for determining of igneous rocks origin (Zhou, 1986) using the microprobe results of biotite.

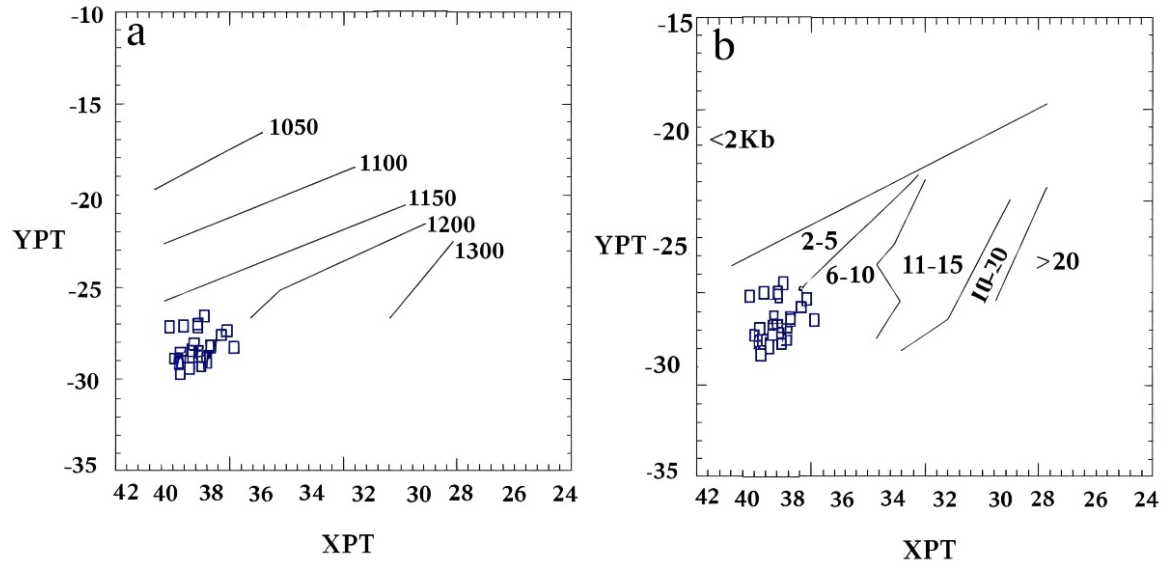

Figure 8. (a) and (b) Thermometric and barometric diagrams based on Soesoo's method (Soesoo, 1997) to determine the temperature and pressure of clinopyroxene formation of the Nusha area intrusives.

the results related to mineral chemistry (of pyroxenes and biotites).

5.2.2 Source and origin characterization

Several hypotheses have been proposed for the origin of high-K calc-alkaline and shoshonite magmatic rocks, including partial melting of the lower continental crust (Bitencourt and Nardi, 2004), AFC processes involving mantle-derived magmas (López-Moro and López-Plaza, 2004), and partial melting of metasomatized lithospheric mantle with phlogopite and amphibole veins (Jiang et al., 2012). However, the geochemical characteristics of Nusha intrusive rocks do not support the first hypothesis, as high-K calc-alkaline and shoshonite magmas derived from the lower continental crust typically contain more than 4 wt.% Na_2O (Xiao and Clemens, 2007), while most Nusha samples contain less than 4 wt.% (Table 1).

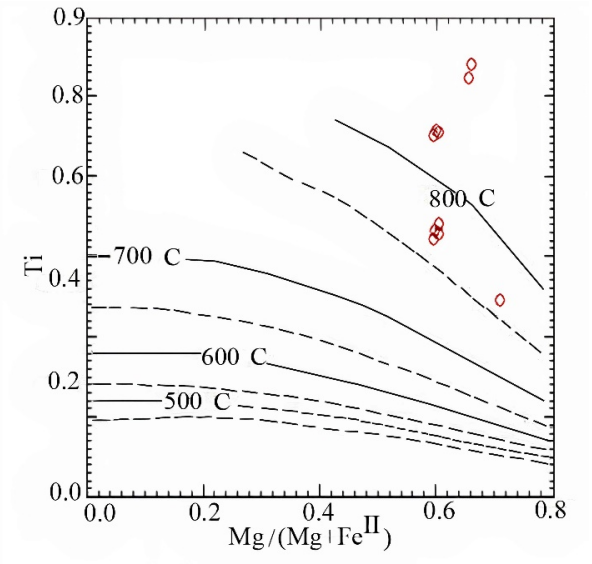

Figure 9. The Ti vs. Mg/(Mg+Fe) diagram (Henry et al., 2005) for determining the crystallization temperature of biotites in the Nusha intrusives.

The Nb/La ratios of Nusha intrusive rocks ($0.4-1.34$) indicate a lithospheric mantle origin ((Bradshaw and Smith, 1994; Smith et al., 1999), ~ 0.3 to 1.2), and their Ce/Pb ratios ($18-1.04$) are significantly different from those of oceanic basalts (e.g., (Hofmann, 1997), ~ 25) further confirming a lithospheric mantle source instead of normal asthenospheric mantle melting. The high LILE and LREE concentrations, and significant negative Nb, Ta, and Ti anomalies, and primitive mantle-normalized spider diagrams (Fig. 6 (d)) suggest that the Nusha intrusive rocks did not originate from typical MORB or OIB sources (which usually show positive Nb-Ti anomalies in multi-element spider diagrams) (e.g., (Hofmann, 1997).

Further support for a lithospheric mantle origin comes from the Nb/Zr ratio (0.76), much lower than the primitive mantle value of 15.71 (Sun and McDonough, 1989), indicating an enriched lithospheric mantle source metasomatized by subduction fluids. The enrichment of LREEs, the positive anomaly of LILEs, and the negative anomaly of HFSEs are considered among the characteristics of magmas originating from the sub-continental metasomatized lithospheric mantle in the subduction zone settings (Pearce, 1982; Foley and Wheller, 1990; Pearce and Parkinson, 1993). The Nb-Zr diagram (Abu-Hamatteh, 2005) also confirms a chemically enriched lithospheric mantle source for the Nusha intrusive rocks (Fig. 11 (a)). Enrichment of the origin zone by subduction components is also seen in the Nb/Y vs. Rb/Y diagram (Temel et al., 1998) (Fig. 11 (b)).

Enrichment and metasomatism of the origin area of arc-related magmas can be caused by the impact of fluids separated from the oceanic crust or melts derived from the partial melting of subducted sediments (Guo et al., 2007). As HFSEs are mostly displaced by aqueous melts, while LILEs are mostly transported by fluids (Herman et al., 2006; Chen et al., 2018), so the dominant factor of metasomatism

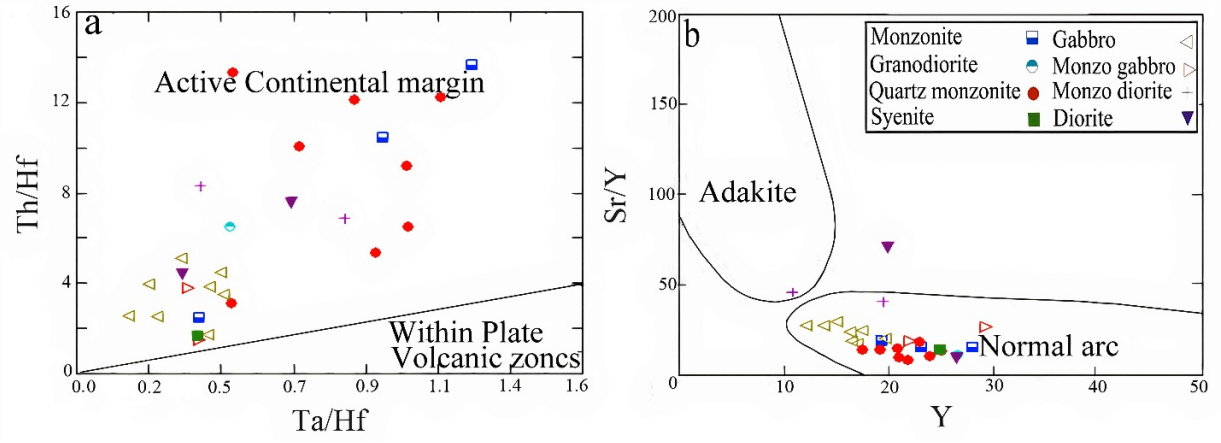

Figure 10. The Nusha area intrusive rocks data plotted on the diagrams: (a) Th/Hf-Ta/Hf (Schandl and Gorton, 2002). According to this diagram, the studied samples are located in the active continental margin field. (b) The Sr/Y vs. Y diagram (Castillo, 2012; Defant and Drummond, 1990). The studied samples are of normal arc types and do not belong to the adakite group.

can be found using the ratio of elements with different mobility properties. The role of fluids in mantle metasomatism is supported by the relatively constant Th/Yb ratio compared to the variable Ba/La ratio, indicating a greater role for fluids than partial melts in the metasomatism process (Fig. 12 (a)).

The residual mineralogy and degree of partial melting in the Nusha lithospheric mantle can be inferred from rare earth element (REE) abundances and ratios. According to Wilson (1989) and Rollinson (1993), LREE enrichment relative to HREE can indicate melt equilibration with garnet as a residual phase. The lower concentration of HREE and Y elements is interpreted as the presence of residual phases in the melt origin. Some authors (such as (Wilson, 1989; Rollinson, 1993; Winter, 2001) also stated that the Y element can be concentrated in garnet and negative Y anomaly is a sign of deep magma origin. La and Sm are not significantly affected by changes in source mineralogy (such as garnet or spinel), so they can provide information on the chemical composition of the source (Aldanmaz et al., 2000). On the Sm/Yb vs. Sm diagram (Fig. 12 (b)), the curves show the changes in the composition of melts derived from the spinel lherzolite and garnet lherzolite source with different degrees of partial melting, and the numbers on these curves represent the degrees of melting.

Nusha area gabbros, the least differentiated rocks according to the Mg numbers, were plotted on the mentioned diagrams to provide a better picture of the nature and melting conditions of the mantle source. In this diagram, the Sm/Yb ratio of the rocks of the studied area is higher than the melting curve of spinel-garnet lherzolite (Gt/Sp = 50:50) and lower than the melting curve of garnet lherzolite, and they often placed in the range where garnet is more than spinel. Thus, the simplest model for the systematic calculation of REE of the studied samples includes garnet + spinel mantle mineralogy (with low to moderate degrees of partial melting). Thus, the source for them was a spinel-garnet lherzolite mantle which has undergone partial melting of about $3-20\%$ degrees.

Enrichment of incompatible elements in mantle wedge can be attributed to the following factors (Rock, 1991): (1) involvement of a metasomatized and abnormal K-rich litho-

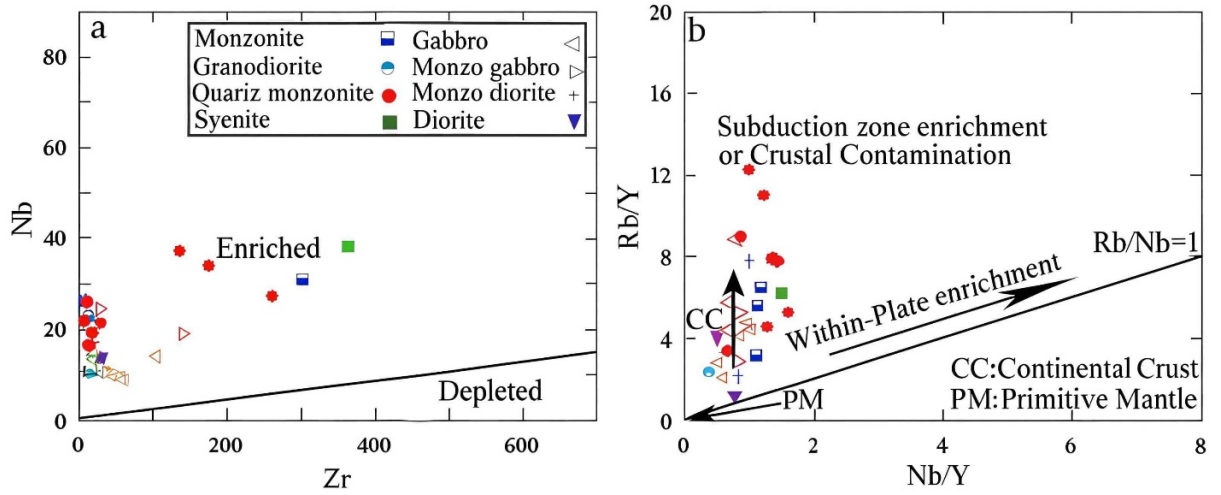

Figure 11. The Nusha area intrusive rocks data plotted on the diagrams: (a) The Nb vs. Zr diagram (Abu-Hamatteh, 2005); and (b) the Nb/Y vs. Rb/Y diagram (Temel et al., 1998) to determine the enrichment or depletion of the origin area.

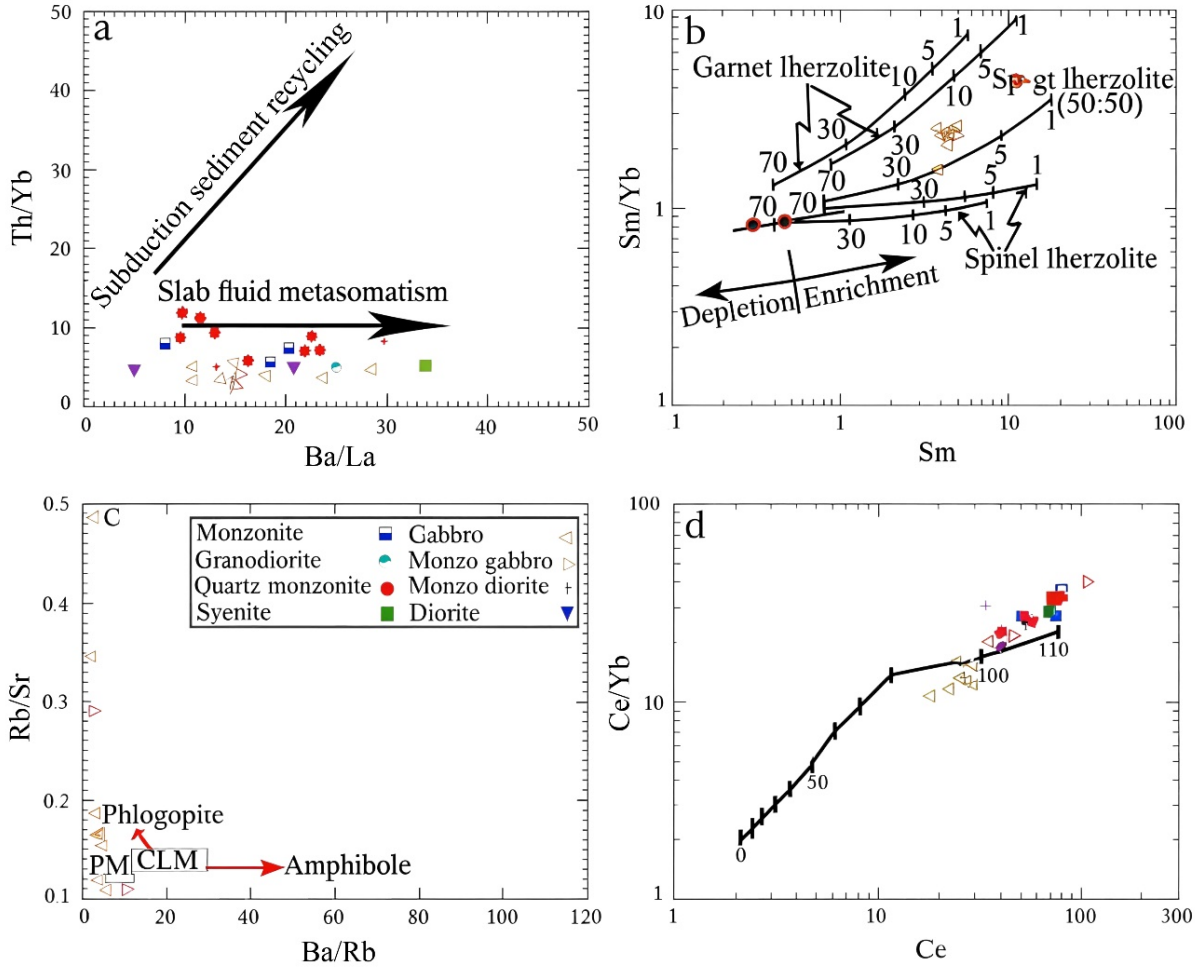

Figure 12. The Nusha intrusives data on the diagram of: (a) Th/Yb vs. Ba/La (Saunders et al., 1992) to discriminate the role of fluids and melts derived from subducting slab. (b) Sm/Yb vs. Sm diagram to identify the nature and degrees of origin partial melting. In these diagrams, the bold arrow, which is related to the enrichment and depletion of the mantle, were defined by McKenzie and O'Nions (1991) and the primary mantle is after Sun and McDonough (1989). The melting curves for spinel lherzolites and garnet peridotites and PM and DM compounds are quoted from Aldanmaz et al. (2000). (c) Rb/Sr vs. Ba/Rb diagram (Furman and Graham, 1999) for gabbroic rocks to identify source mineralogy. Nusha data are more consistent with the presence of phlogopite in the source. (d) The Ce/Yb vs. Ce (Ellam and Cox, 1991) plot for evaluating the depth of melting source. As can be seen in this diagram, the melting depth of the origin of the studied rocks is between 85 and $\sim$ 110 km.

spheric mantle zone, (2) recycling of a crust component in subduction zones (e.g., (Tatsumi and Eggins, 1995; Jahn et al., 1999)). Melts in equilibrium with a phlogopite-bearing source have Rb/Sr>0.1 and Ba/Rb $<$ 15, while those in equilibrium with amphibole-bearing source Rb/Sr $<$ 0.06 and Ba/Rb $>$ 15 (Furman and Graham, 1999). The Nusha gabbros exhibit Rb/Sr (0.01 – 1.34) and Ba/Rb (1.55 – 10.82) ratios that are consistent with a phlogopite-bearing source (Fig. 12 (c)).

REE ratios are good indicators of melting depth since fractional crystallization does not affect them greatly (Ellam and Cox, 1991). Melting depth estimates, based on REE ratios like Ce/Yb, suggest that the Nusha magma originated at depths of $\sim$ 85 to $\sim$ 110 km (Fig. 12 (d)). Experimental data indicate that shoshonitic magmas require higher pressures (2 – 3 GPa) than basanite magmas (Wang et al., 1991), suggesting that the Nusha intrusions formed from the melting of spinel-garnet lherzolite at a depth corresponding to a lithospheric mantle wedge.

5.2.3 Crustal contamination

Crustal contamination and assimilation are most likely where the magma ascends slowly and the thickness of the crust is high, allowing it to interact with the crust for longer periods (Furman, 2007). The Mg numbers (20 – 64) of the Nusha intrusions indicate that the magma evolved significantly, as primary melts in arc zones generally have Mg numbers above 70 (Schmidt and Jagoutz, 2017). Lots of geochemical evidences support contamination of Nusha intrusion magma with continental crust. Geochemical evidence of crustal contamination includes enrichment in large-ion lithophile elements (LILE) such as Pb, Ba, and Rb, while high-field strength elements (HFSE) remain relatively unchanged (Furman, 2007) (Fig. 6 (d)).

Ce/Pb in mafic rocks is sensitive to contamination, making it a useful indicator of crustal assimilation (Furman, 2007). Crustal contamination of the Nusha data is supported by this indicator (Fig. 13 (a)). Nb/U (Furman, 2007) ratios is another sensitive indicator to crustal contamination. The low values of the mentioned ratio are mostly due to the

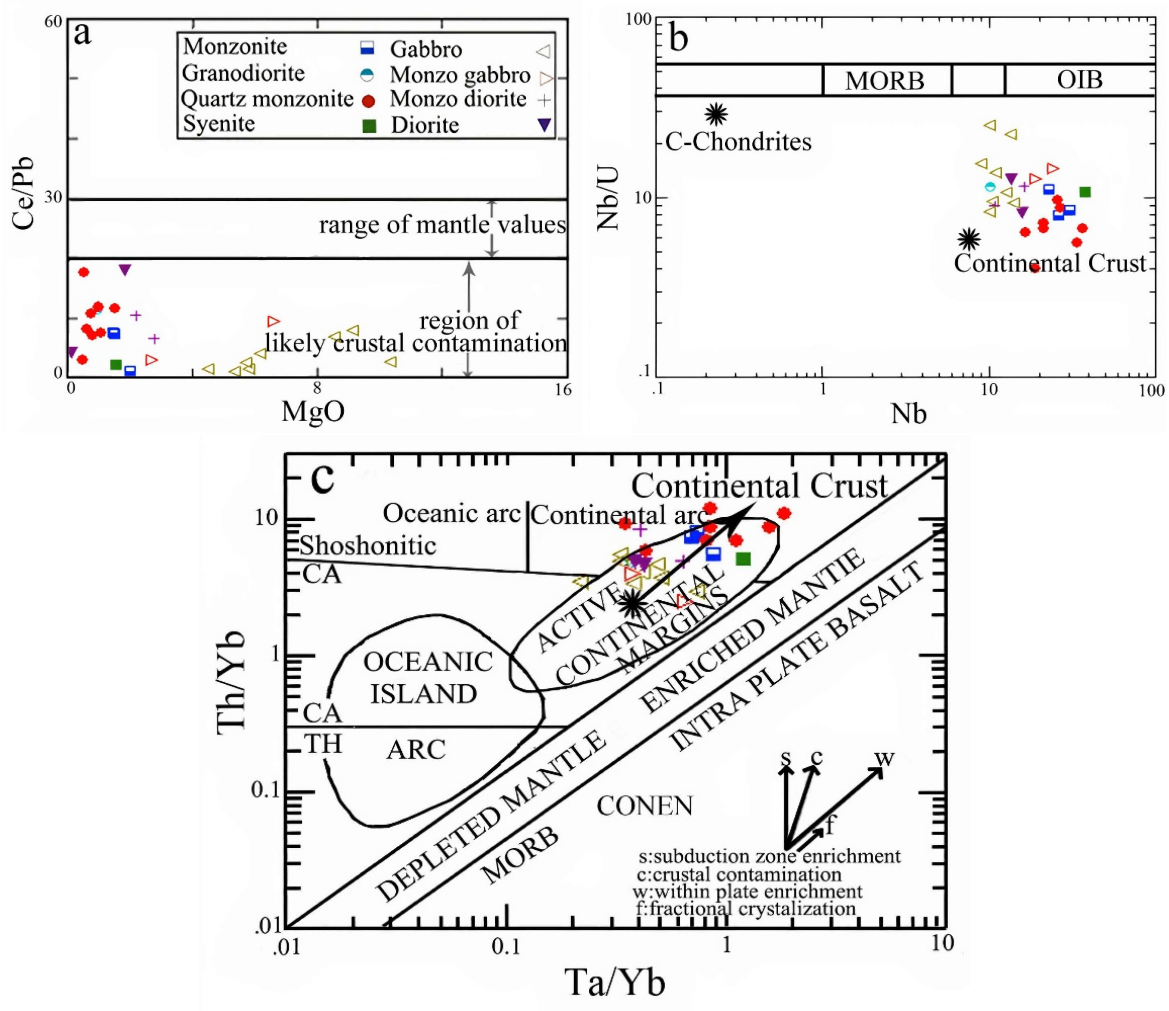

Figure 13. Nusha intrusives data on: (a) The Ce/Yb-MgO (Furman, 2007) diagram on which samples are placed in the crustal contamination range. (b) The Nb/U vs. Nb (Cornelius et al., 2011) diagrams respectively which indicate the composition similarity of continental crust due to the effect of crustal contamination on them. (c) Th/Yb vs. Ta/Yb (Pearce, 1983) in which the samples of the studied rocks are located near but above the continental crust in the continental arc zone and outside the mantle array. The position of the mantle and crustal members is from Pearce (2008) and Pearce and Peate (1995) and the average crust is from Rudnick and Gao (2003).

small content of Nb compared to U in the continental crust. The Nb poverty in the continental crust can caused by two reasons. First, Nb, like Ti, mostly remains in Ti-bearing minerals and amphibole in the subducted crust and prevents it from entering the melt and the subsequent crustal formation processes (Hofmann, 1997). Second, Nb is transported only by silicate melts and not by subduction fluids (Pearce and Peate, 1995). Based on Rollinson (1993) the negative Nb anomaly is mostly an indicator of the involvement of the continental crust in magmatic processes. The low value of the Nb/U ratio in the studied samples is similar to the mean values of the continental crust, indicating the effect of crustal contamination (Fig. 13 (b)). Additionally, relatively high values of some LILE elements and high Ba/Nb ratios confirm the effect of crustal components in the formation of these rocks when magma rises through the crustal rocks. The positive anomaly of K, Pb, and generally, the enrichment of LIL elements is attributed to crustal contamination of magmas (Taylor and McLennan, 1985; Hofmann, 1997; Roy et al., 2002; Girardi et al., 2012). Also, LIL elements are concentrated in the continental crust (Rollinson, 1993), and their high concentration in Nusha intrusive rocks can indicate crustal contamination.

Distinguishing the effects of crustal contamination on magma compositions from the results of metasomatism caused by subduction processes is often difficult (Aldanmaz et al., 2000). Th/Yb vs. Ta/Yb diagram (Pearce, 2008), with samples plotting outside the mantle array and higher Th/Yb than continental crust (Fig. 13 (c)), confirm crustal contamination is not the only evolution process during magma ascent. This can point to different processes such as fractional crystallization, partial melting, and AFC acting on a magma derived from a metasomatized mantle by a subduction component. According to the Nb/Y vs. Rb/Y diagram (Temel et al., 1998), the studied samples experienced enrichment and crustal contamination in the subduction zone (Fig. 11 (b)). The Rb vs. Ba/Rb diagram (Askren et al., 1997) clarifies the role of crustal contamination with fractional crystallization in the upper crust (Fig. 14 (a)). Tchameni et al. (2006) used the Rb/Th vs. Rb variation diagram to distinguish fractional crystallization (FC), crustal contamination (CC), and assimilation

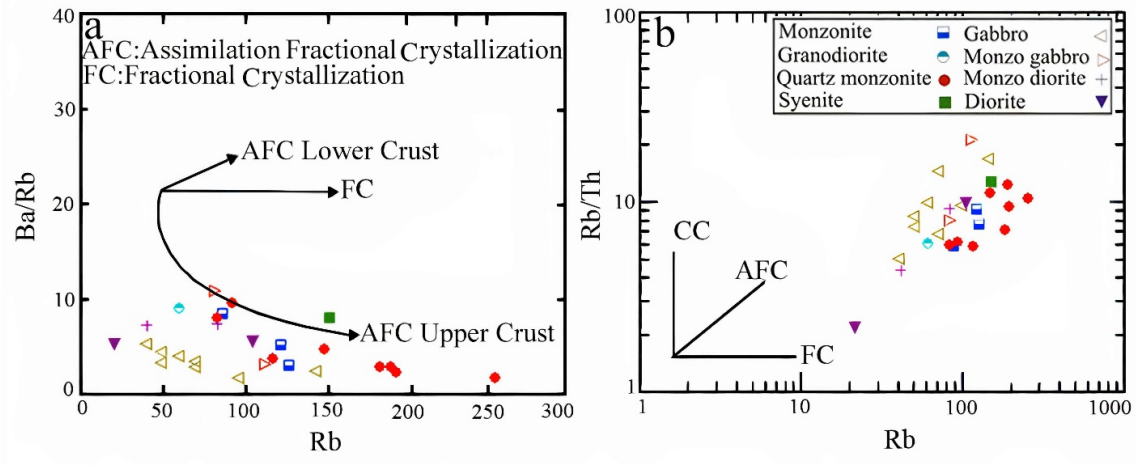

Figure 14. Nusha intrusive samples plotted on: (a) The Rb vs. Ba/Rb diagram (Askren et al., 1997), and (b) The Rb vs. Rb/Th ratio (Tchameni et al., 2006).

and fractional crystallization (AFC) in rocks. In this diagram, the studied samples show an almost diagonal trend, indicating the process of assimilation-fractional crystallization (AFC) in the magmatic evolution of the studied rocks (Fig. 14 (b)). This means that the magma after passing through the enriched lithospheric mantle in the subsurface magma chambers has also undergone the AFC process. The results obtained from the microprobe data also confirm this issue so that the chemical composition of biotites shows that the origin of Nusha intrusive rocks was a mixture of crust and mantle materials (Fig. 7 (f)).

5.2.4 Geodynamics

Many studies suggest that the Alborz and Urumieh-Dokhtar magmatic belts are both discrete parts of the magmatic arc of the Neo-Tethys unit (Axen et al., 2001). The Alborz magmatic assemblage is attributed to the subduction of the Neo-Tethys oceanic lithosphere beneath Central Iran, following the collision of the Arabian continent and the Iranian microcontinent in late Cretaceous-early Cenozoic (Berberian and Berberian, 1981; Berberian et al., 1982; Alavi, 1996; Golonka, 2004). Although the Cenozoic magmatic rocks of Alborz show arc magma characteristics, there is substantial evidence that much of Iran, including the Alborz region, experienced extensional tectonics during part of the Eocene (Verdel et al., 2011; Mouthereau et al., 2012). The presence of Eocene normal faults in Alborz mountains (Guest et al., 2006), stratigraphic evidence of Eocene subsidence in Alborz mountains and Central Iran (Brunet et al., 2003; Hassanzadeh et al., 2004; Vincent et al., 2005; Morley et al., 2009), the existence of interbedded shallow marine sediments throughout the Paleogene volcanic succession (Stöcklin, 1968; Berberian and Berberian, 1981), proof of submarine volcanic activity (e.g., (Förster et al., 1972; Amidi et al., 1984; Spies et al., 1984; Hassanzadeh, 1993)), and the occurrence of primary basalts in Alborz (north of Karaj and Meshkin) with characteristics contrary to the volcanic arc (and with asthenosphere origins, such as lack of relative depletion of Zr and Nb and positive anomaly of Sr) (Asiabanha and Foden, 2012) have led to presenting different opinions about the Cenozoic geodynamics of Alborz. Some of which are listed below.

An extensional back-arc basin caused by the deep subduction of the Arabian plate beneath the Central Iran plate (Roohbakhsh et al., 2018; Alavi, 1996; Azizi and Jahangiri, 2008), the initial stages of a back-arc basin but completely affected by the characteristics of arc magmas (Teimouri, 2011; Asiabanha and Foden, 2012), Neo-Tethys subduction in the form of an oblique convergence between the Arabian plate and central Iran plate with a weak subduction interface rather than in an orthogonal convergence and strong subduction interface (Upton et al., 2003; Ashrafi et al., 2018), slab roll-back as a result of the high slab dipping angle in the long-term period (Upper Cretaceous to Paleogene) (Moghadam et al., 2018; Moghadam and Stern, 2011), the slab roll-back and retreat after the Cretaceous period with the flat subduction of the slab, similar to Laramide and post-Laramide evolution in the western United States (Verdel et al., 2011), subducting slab break-off (Davies and Blanckenburg, 1995), drip or delamination-related magmatism of lithosphere (Bird, 1979), and local tensile strengths due to post-collision regime (Kearey and Vine, 1996; Einsele, 2000).

The Nusha intrusions, geochemically non-adakite high-K calc-alkaline and shoshonitic, originated from an enriched lithospheric mantle source that underwent partial melting at a depth of $85-110$ km. The magma was then contaminated with the continental crust during its ascent. The long-term nature of magmatic events in the convergent margin of Iran and the irregular but widespread patterns of magmatism during the Mesozoic to late Paleogene are not consistent with drip or delamination-related magmatism or subducting slab break-off (Sepidbar et al., 2019). Furthermore, the delamination phenomenon leads to a reduced thickness of the lithosphere, and this is in contrast with the Nusha lithospheric mantle, which is about 110 km thick. Slab break-off mostly leads to the creation of adakite magma (Sepidbar et al., 2019), which is in contrast to the nature of Nusha intrusions. The great distance between Nusha and the subduction suture zone of Neo-Tethys oceanic crust beneath the subcontinent of Central Iran ($>$ 300 km) also excludes deep

subduction with a moderate and steady slope. Thus, given what was stated and the studies conducted on the activity of Eocene-Oligocene magmatism in Alborz and the studied area, the third stage in the model presented by Verdel et al. (2011), which is similar to the model of Humphreys et al. (2006) (concerning mid-Tertiary magmatism in the western United States) is more consistent with the facts of the Nusha and central Alborz intrusions.

This proposed model for the formation of the Nusha intrusive rocks includes four stages: (1) Steep subduction of the oceanic crust at the end of the Triassic, preparing the lithosphere located in the north of the Arabia-Eurasia suture for volcanic arc activity. (2) Just after the Aptian-Albian orogenic phase, low-angle subduction during the Late Cretaceous, leading to magmatic activity in Central Iran and the Alborz region. A series of tectonic contractions occurred in Iran toward the north of this structural zone at the end of the Cretaceous. Furthermore, the preparation of the upper mantle extends to the Alborz Mountains and northern Iran in this stage. (3) Extensional tectonics and thinning of the crust along with the slab rollback during the Eocene, resulting in decompression melting of the preconditioned mantle. Numerous reasons support rollback, subduction speed, slab age, differences between the slab and mantle densities, and so on (Heuret and Lallemand, 2005). Partial melting mostly occurred in the hydrated lithospheric mantle caused by combined effect of the decompression and heat from the upwelling of the asthenosphere. In this stage, volcanic sequences and shallow marine sediments were accumulated in extensional environments (Fig. 15). (4) Replacing of thinned lithosphere by upwelled asthenosphere at the beginning of the Oligocene, caused limited partial melting in the asthenosphere in the back-arc basin (Gribble et al., 1998).

6. Conclusion

Based on the information obtained from field, petrography, whole-rock and the microprobe chemical analyses of Nusha intrusives, the following conclusions can be presented:

- Petrographically, they have gabbronorite, gabbro, monzogabbro, diorite, syenite, monzonite, monzodiorite, granodiorite, and quartz monzonite compositions.

– Based on microprobe data the pyroxene compositions are mostly augite and salite, and orthopyroxenes are hypersthene. The data obtained from geothermobarometry of clinopyroxenes show that their crystallization often occurred at pressures of 6 to 7 kb and temperature of 1170 to 1210 °C.

– Geochemically the intrusive rocks of the Nusha are mostly high-K calc-alkaline and shoshonitic with non-adakitic nature.

– Geochemical evidences such as enrichment in LILE and LREE and low concentration of HREE and HFSE and negative anomaly of Zr, Nb, and Ti, along with positive anomaly of K, LILE and tectonomagmatic discriminating diagrams indicate that the Nusha intrusives belonged to active continental margin.

– The behavior of rare elements such as Nb and Zr indicate that their parental magma has many compositional similarities with melts originated from an enriched lithospheric mantle.

– Using the ratio of elements with different mobility properties, it was found that the fluids derived from the subducting plate played a more significant role in mantle metasomatism than the partial melts originated from the subducting sediments.

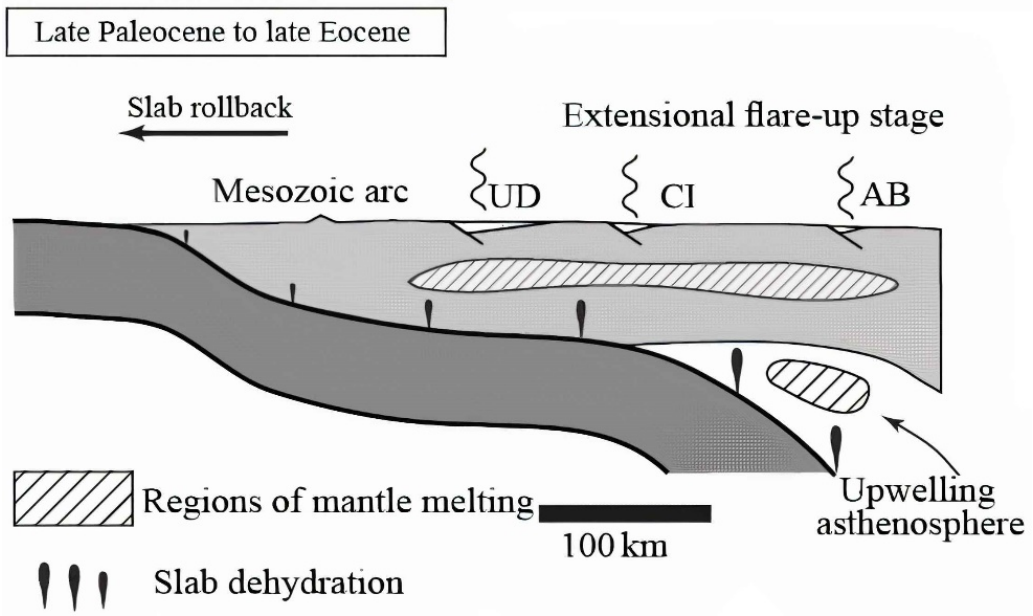

Figure 15. An illustration of the evolution of Iran's structural zones from the late Paleocene to the late Eocene, in which the slab rollback thinned the overriding plate and led to decompression melting of the enriched lithospheric mantle and developing of the back-arc basins. UD: Urumieh-Dokhtar, CI: Central Iran, AB: Alborz Belt, (Verdel et al., 2011).

– The abundance and proportions of rare earth elements showed that the parental magma was formed from the 3 to 20% degrees of partial melting of an enriched spinel garnet-lherzolite lithospheric mantle source which contains phlogopite at a depth of 85 to slightly more than 110 km.

– Lots of geochemical evidences such as significant enrichment of large ion lithophile elements (LILE) compared to HFSE, elemental ratios like Ce/Pb and Nb/U, and the chemical compositions of biotites indicate that Nusha magma has been contaminated with continental crust during its ascend and undergone the AFC process.

– Geodynamically the Nusha intrusives belonged to an arc setting of subducting Neo-Tethyan oceanic lithosphere in an extensional environment.

Authors contributions
Authors have contributed equally in preparing and writing the manuscript.

Availability of data and materials
The data that support the findings of this study are available from the corresponding author, upon reasonable request.

Conflict of interests
The authors declare that they have no known competing financial interests or personal relationships that could have appeared to influence the work reported in this paper.

References

Abdel-Rahman A. F. M. (1994) Nature of biotites from alkaline, calc-alkaline, and peraluminous magmas. *Journal of Petrology* 35 (2): 525–541. DOI: https://doi.org/10.1093/petrology/35.2.525.

Abdolahadi A., Sheikhzakariaee S. J., Yazdi A., Mousavi S. Z. (2025) Plio-Quaternary Adakite Genesis and Post-collisional Processes: Whole Rock Constraints and Sr, Nd Isotopic Compositions in Alborz Magmatic Belt, Ardabil, Iran. *Journal of Mining and Environment* 16 (2): 737–765. DOI: https://doi.org/10.22044/jme.2024.14781.2801.

Abu-Hamatteh H. Z. S. H. (2005) Geochemistry and petrogenesis of mafic magmatic rocks of the Jharol Belt, India: geodynamic implication. *Journal of Asian Earth Sciences* 25:557–581. DOI: https://doi.org/10.1016/j.jseaes.2004.05.006.

Aghazadeh M. (2009) Petrology and Geochemistry of Anzan, Khankandi and Shaivar Dagh granitoids (North and East of Ahar, Eastern Azerbaijan) with references to associated mineralization. *Unpublished Ph.D thesis, Tarbiat Moddares University, Iran,* 470.

Aghazadeh M., Hou Z., Badrzadeh Z. (2013) Bondar-e-Honza: An Oldest and Special Porphyry Copper (Molybdenum) Deposit in the Kerman Porphyry Copper Belt, Iran. *Mineral Deposit Research for a High-Tech World, 12th SGA Biennial Meeting, Uppsala, Sweden* 3:1412–1415.

Alavi M. (1996) Tectonostratigraphy synthesis and structural style of the Alborz Mountain system in northern Iran. *Journal Geodynamics* 21:1–33. DOI: https://doi.org/10.1016/0264-3707(95)00009-7.

Aldanmaz E., Pearcea J. A., Thirlwall M. F., Mitchell J. G. (2000) Petrogenetic evolution of late Cenozoic, post-collision volcanism in western Anatolia. *Turkey Journal of Volcanology and Geothermal Research* 102:67–95. DOI: https://doi.org/10.1016/S0377-0273(00)00182-7.

Amidi S. M., Emami M. H., Michel R. (1984) Alkaline character of Eocene volcanism in the middle part of Iran and its geodynamic situation. *Geologische Rundschau* 73:917–932. DOI: https://doi.org/10.1007/BF01820882.

Annells R. N., Arthurton R. S., Bazley R. A., Davies R. G. (1975) Geologic map of Qazvin and Rasht quadrangle, 1:250000 *Geological Survey and Mineral exploration of Iran*

Arjmandzadeh R., Almasi A., Nabatian G., Li Q., Nourian S., Jafarie T. (2022) Zircon U–Pb dating, geochemistry, and geology of Shotorsang hypabyssal granitoids, southern Quchan (northeast of Iran). *Petrological Journal* 13 (3): 105–130. DOI: https://doi.org/10.22108/ijp.2022.132228.1263.

Ashrafi N., Dabiri R., Jahangiri A. (2024) Some chemical variations in biotite, phlogopite, and muscovite, considering their tectonic setting. *Geopersia* 14 (2): 307–325. DOI: https://doi.org/10.22059/geope.2024.373882.648749.

Ashrafi N., Jahangiri A., Hasebe N., Eby G. N. (2018) Petrology, geochemistry and geodynamic setting of Eocene-Oligocene alkaline intrusions from the Alborz-Azerbaijan magmatic belt, NW Iran. *Geochemistry* 78:432–461. DOI: https://doi.org/10.1016/j.chemer.2018.10.004.

Asiabanha A., Foden J. (2012) Post collisional transition from an extensional volcano sedimentary basin to a continental arc in the Alborz Ranges, N-Iran. *Lithos* 148:98–111. DOI: https://doi.org/10.1016/j.lithos.2012.05.014.

Asiabanha A., Ghasemi H., Meshkin M. (2009) Paleogene continental-arc type volcanism in North Qazvin, North Iran: Facies analysis and geochemistry. *Neues Jahrbuch Fur Mineralogie-Abhandlungen* 186 (2): 201–214. DOI: https://doi.org/10.1127/0077-7757/2009/0144.

Askren D. R., Roden M. F., Whitney J. A. (1997) Petrogenesis of Tertiary andesite lava flows interlayered with large-volume felsic ash-flow tuffs of the western USA. *Journal of Petrology* 38 (8): 1021–1046. DOI: https://doi.org/10.1093/petroj/38.8.1021.

Axen G. J., Lam P. S., Grove M., Stockli D. F., Hassanzadeh J. (2001) Exhumation of the west-central Alborz mountains, Iran, Caspian subsidence, and collision-related tectonics. *Journal Geology* 29 (6): 559–562. DOI: https://doi.org/10.1130/0091-7613(2001)0290559:EOTWCA2.0.CO;2.

Azizi H., Jahangiri A. (2008) Cretaceous subduction-related volcanism in the northern Sanandaj-Sirjan Zone, Iran. *Journal of Geodynamics* 45:178–190. DOI: https://doi.org/10.1016/j.jog.2007.11.001.

Azizi H., Tsuboi M. (2021) The Van Microplate: A New Microcontinent at the Junction of Iran, Turkey, and Armenia. *Frontiers in Earth Science* 8:1–15. DOI: https://doi.org/10.3389/feart.2020.574385.

Bahajroy M., Taki S., Moazzen M., Ganji A. (2022) Whole rock and mineral chemistry of intermediate intrusive rocks on the northern side of Shahroud River near Zardkooh in Guilan province (Iran). *Petrological Journal* 13 (3): 1–32. DOI: https://doi.org/10.22108/ijp.2022.132420.1267.

Baharfiruzi K., Shafieii A., Azhdari H., Karimi H. (2001) Geologic map of Javaherdeh, 1:100000. *Geological Survey and Mineral exploration of Iran.,* 6064.

Ballèvre M., Le Goff E., Hébert R. (2001) The tectonothermal evolution of the Cadomian belt of northern Brittany, France: a Neoproterozoic volcanic arc. *Tectonophysics* 331 (1-2): 19–43. DOI: https://doi.org/10.1016/S0040-1951(00)00234-1.

Berberian F., Berberian M. (1981) Tectono-plutonic episodes in Iran. *Himalaya Geodynamic Evolution. American Geophysical Union, Washington DC,* 5–32.

Berberian F., Muir I. D., Pankhurst R. J., Berberian M. (1982) Late Cretaceous and early Miocene Andean type plutonic activity in northern Makran and central Iran. *Journal of the Geological Society* 139 (5): 605–614. DOI: https://doi.org/10.1144/gsjgs.139.5.0605.

Bird P. (1979) Continental delamination and the Colorado Plateau. *Journal of Geophysical Research: Solid Earth* 84:7561–7571. DOI: https://doi.org/10.1029/JB084iB13p07561.

Bitencourt M. F., Nardi L. V. S. (2004) The role of xenoliths and flow segregation in the genesis and evolution of the Paleoproterozoic Itapema Granite, a crustally derived magma of shoshonitic affinity from southern Brazil. *Lithos* 73:1–19. DOI: https://doi.org/10.1016/j.lithos.2003.08.004.

Bradshaw T. K., Smith E. I. (1994) Polygenetic Quaternary volcanism at Crater Flat, Nevada. *Journal of Volcanology and Geothermal Research* 63:165–182. DOI: https://doi.org/10.1016/0377-0273(94)90072-8.

Brunet M. F., Korotaev M. V., Ershov A. V., Nikishin A. M. (2003) The South Caspian basin: A review of its evolution from subsidence modeling. *Sedimentary Geology* 156:119–148. DOI: https://doi.org/10.1016/S0037-0738(02)00285-3.

Castillo P. R. (2012) Adakite petrogenesis. *Lithos* 134-135:304–316. DOI: https://doi.org/10.1016/j.lithos.2011.09.013.

Chen L., Zheng Y. F., Zhao Z. F. (2018) A common crustal component in the sources of bimodal magmatism: geochemical evidence from Mesozoic volcanics in the Middle-Lower Yangtze Valley, South China. *Journal of Geological Society of America Bulletin* 130:1959–1980. DOI: https://doi.org/10.1130/B31856.1.

Cornelius T., Ntaflos T. H., Akinin V. (2011) Polybaric petrogenesis of Neogene alkaline magmas in an extensional tectonic environment: Viliga Volcanic Field, northeast Russia. *Lithos* 122:13–24. DOI: https://doi.org/10.1016/j.lithos.2010.11.009.

Dabiri R., Akbari-Mogaddam M., Ghaffari M. (2018) Geochemical evolution and petrogenesis of the Eocene Kashmar granitoid rocks, NE Iran: Implications for fractional crystallization and crustal contamination processes. *Iranian Journal of Earth Sciences* 10 (1): 68–77.

Darvishzadeh A. (1991) Geology of Iran. *Amir Kabir Publishing co., Tehran,* 901.

Davies J. H., Blanckenburg F. von (1995) Slab breakoff: A model of lithosphere detachment and its test in the magmatism and deformation of collisional orogens. *Earth and Planetary Science Letters* 129:85–102. DOI: https://doi.org/10.1016/0012-821X(94)00237-S.

Deer W. A., Howie R. A., Zussman J. (1991) An introduction to the rock-forming minerals. *Longman Scientific Technical, New York* 528

Defant M. J., Drummond M. S. (1990) Derivation of some modern magmas by melting of young subducted lithosphere. *Nature* 347:662–665. DOI: https://doi.org/10.1038/347662a0.

Einsele G. (2000) Sedimentary Basins: Evolution, Facies and Sediment Budget. *Second edition. Springer-Verlag. Berlin.,* 792.

Ellam R. M., Cox K. G. (1991) An interpretation of Karoo picrate basalts in terms of interaction between asthenospheric magmas and the mantle lithosphere Earth. *Planet Science Letter* 105:330–342. DOI: https://doi.org/10.1016/0012-821X(91)90141-4.

Foley S., Peccerillo A. (1992) Potassic and ultrapotassic magmas and their origin. *Lithos* 28 (3-6): 181–185. DOI: https://doi.org/10.1016/0024-4937(92)90005-J.

Foley S. F., Wheller G. E. (1990) Parallels in the origin of the geochemical signatures of island arc volcanics and continental potassic igneous rocks: the role of residual titanites. *Chemical Geology* 85 (1-2): 1–18. DOI: https://doi.org/10.1016/0009-2541(90)90120-V.

Forster M. D. (1960) Interpretation of the composition of trioctahedral mica. *American Geological Survey, Professional Paper* 354B:1–48.

Furman T. (2007) Geochemistry of East African Rift basalts: an overview. *Journal of African Earth Sciences* 48 (2): 147–160. DOI: https://doi.org/10.1016/j.jafrearsci.2006.06.009.

Furman T., Graham D. (1999) Erosion of lithospheric mantle beneath the East African Rift system: geochemical evidence from the Kivu volcanic province. *Lithos* 48:237–262. DOI: https://doi.org/10.1016/S0024-4937(99)00031-6.

Förster H., Fesefeldt K., Kürsten M. (1972) Magmatic and orogenic evolution of the central Iranian volcanic belt. *24th International Geologic Congress,* 198–210.

Gass I. G., Lippard S. J., Shelton A. W. (1984) Ophiolites and Oceanic Lithosphere. *Geological Society Special Publication, London,* 413. DOI: https://doi.org/10.1002/gj.3350200310.

Ghasempour M. R., Ghazi J. M., Biabangard H., Dabiri R. (2014) Petrogenic significance of the Plio-Quaternary Nehbandan mafic lavas, Eastern Iran. *Iranian Journal of Earth Sciences* 6:133–141.

Girardi J. D., Patchett P. J., Ducea M. N., Gehrels G. E., Cecil M. R. (2012) Elemental and isotopic evidence for granitoid genesis from deep-seated sources in the Coast Mountains batholith, British Columbia. *Journal of Petrology* 53 (7): 1505–1536. DOI: https://doi.org/10.1093/petrology/egs024.

Golonka J. (2004) Plate tectonic evolution of the southern margin of Eurasia in the Mesozoic and Cenozoic. *Tectonophysics* 381 (1-4): 235–273. DOI: https://doi.org/10.1016/j.tecto.2002.06.004.

Gribble R. F., Stern R. J., Newman S., Bloomer S. H., O'Hearn T. (1998) Chemical and isotopic composition of lavas from the northern Mariana trough: Implications for magma genesis in back-arc basins. *Journal of Petrology* 39:125–154. DOI: https://doi.org/10.1093/petrology/39.1.125.

Guest B., Axen G. J., Lam P. S., Hassanzadeh J. (2006) Late Cenozoic shortening in the west-central Alborz mountains, northern Iran, by combined conjugate strike-slip and thin-skinned deformation. *Geosphere* 2:35–52. DOI: https://doi.org/10.1130/GES00019.1.

Guo Z., Wilson M., Liu J. (2007) Post-collisional adakites in south Tibet Products of partial: melting of subduction-modified lower crust. *Lithos* 96:205–224. DOI: https://doi.org/10.1016/j.lithos.2006.09.011.

Hassanzadeh J. (1993) Metallogenic and Tectonomagmatic Events in the SE Sector of the Cenozoic Active Continental Margin of Iran (Shahre-Babak Area, Kerman Province). *Ph.D. Thesis, University of California, Los Angeles,* 204.

Hassanzadeh J., Axen G., Guest B., Stockli D. F., Ghazi A. M. (2004) The Alborz and NW Urumieh-Dokhtar magmatic belts, Iran: Rifted parts of a single ancestral arc. *Geological Society of America, Abstract Programs* 36:434.

Henry D. J., Guidotti C. V., Thomson J. A. (2005) The Ti-Saturation Surface for Low-To-Medium Pressure Metapelitic Biotites: Implications for Geothermometry and Ti-Substitution Mechanisms. *American Mineralogist* 90 (2-3): 316–328. DOI: https://doi.org/10.2138/am.2005.1498.

Herman J., Spindler C., Hack A., Korsakov A. V. (2006) Aqueous fluids and hydrous melts in high pressure and ultra-high-pressure rocks: Implications for element transfer in subduction zones. *Lithos* 92:399–417. DOI: https://doi.org/10.1016/j.lithos.2006.03.055.

Heuret A., Lallemand S. (2005) Plate motions, slab dynamics and back-arc deformation. *Physics of The Earth and Planetary Interiors* 149:31–51. DOI: https://doi.org/10.1016/j.pepi.2004.08.022.

Hofmann A. W. (1997) Mantle geochemistry: the message from oceanic volcanism. *Nature* 385:219–229. DOI: https://doi.org/10.1038/385219a0.

Humphreys M. C. S., Blundy J. D., Sparks S. J. (2006) Magma evolution and open system processes at Shiveluch volcano: insights from phenocryst zoning. *Journal of Petrology* 47 (12): 2303–2334. DOI: https://doi.org/10.1093/petrology/egl045.

Irvine T. N., Baragar W. R. A. (1971) A guide to the chemical classification of the common volcanic rocks. *Canadian Journal Earth Sciences* 8 (5): 523–548. DOI: https://doi.org/10.1139/e71-055.

Jahn B. M., Wu F., Lo C. H., Tsa I. C. H. (1999) Crust-mantle interaction induced by deep subduction of the continental crust: geochemical and Sr-Nd isotopic evidence from post-collisional mafic-ultramafic intrusions of the northern Dabie Complex, central China. *Chemical Geology* 157:119–146. DOI: https://doi.org/10.1016/S0009-2541(98)00197-1.

Jiang Y. H., Liu Z., Jia R. Y., Liao S. Y., Zhou Q., Zhao P. (2012) Miocene potassic granite-syenite association in western Tibetan Plateau: Implications for shoshonitic and high Ba-Sr granite genesis. *Lithos* 134-135:146–162. DOI: https://doi.org/10.1016/j.lithos.2011.12.012.

Kearey P., Vine F. J. (1996) Global Tectonics. *Blackwell Publication, London* 220

Le Bas M. J. (1962) The role of aluminum in igneous clinopyroxenes with relation to their parentage. *American Journal of Science* 260:267–288. DOI: https://doi.org/10.2475/AJS.260.4.267.

Leterrier J., Maury R. C., Thonon P., Girard D., Marchal M. (1982) Clinopyroxene composition as a method of identification of the magmatic affinities of paleo-volcanic series. *Earth and Planetary Science Letters* 59:139–154. DOI: https://doi.org/10.1016/0012-821X(82)90122-4.

Liang Y., Deng J., Liu X., Wang Q., Qin C., Li Y., Yang Y., Zhou M., Jiang J. (2018) Major and trace element, and Sr isotope compositions of clinopyroxene phenocrysts in mafic dykes on Jiaodong Peninsula, southeastern North China Craton: Insights into magma mixing and source metasomatism. *Lithos* 302-303:480–495. DOI: https://doi.org/10.1016/j.lithos.2018.01.031.

López-Moro F. J., López-Plaza M. (2004) Monzonitic series from the Variscan Tormes Dome (Central Iberian Zone): petrogenetic evolution from monzogabbro to granite magmas. *Lithos* 72:19–44. DOI: https://doi.org/10.1016/j.lithos.2003.08.002.

McDonough W. F., Sun S., Ringwood A. E., Jagoutz E., Hofmann A. W. (1992) Potassium, Rubidium, and Cesium in the Earth and Moon and the evolution of the earth's mantle. *Geochimica et Cosmochimica Acta* 56 (3): 1001–1012. DOI: https://doi.org/10.1016/0016-7037(92)90043-I.

McKenzie D., O'Nions R. K. (1991) Partial melt distributions from inversion of rare earth element concentrations. *Journal of Petrology* 32:1021–1091. DOI: https://doi.org/10.1093/petrology/32.5.1021.

Moghadam H. S., Griffin W. L., Kirchenbaur M., Garbe-Schnoberg D., Khedr M. Z., Kimura J. I., Stern R. J., Ghorbani G., Murphy R. C., O'Reilly S. Y. (2018) Roll-back, extension and mantle upwelling triggered Eocene potassic magmatism in NW Iran. *Journal of Petrology* 59:1417–1465. DOI: https://doi.org/10.1093/petrology/egy067.

Moghadam H. S., Stern R. J. (2011) Geodynamic evolution of Upper cretaceous Zagros ophiolites: formation of oceanic lithosphere above a nascent subduction zone. *Geological Magazine* 148:762–801. DOI: https://doi.org/10.1017/S0016756811000410.

Mokhtari M. A. A., Moinvaziri H., Ghorbani M. R., Mehrpartou M. (2010) Petrology and petrogenesis of Kamtal intrusion, Eastern Azarbaijan, NW Iran. *Central European Geology* 53 (1): 79–96. DOI: https://doi.org/10.1556/ceugeol.53.2010.1.5.

Mollai H., Dabiri R., Torshizian H. A., Pe-Piper G., Wang W. (2021) Upper Neoproterozoic garnet-bearing granites in the Zeber-Kuh region from east central Iran micro plate: Implications for the magmatic evolution in the northern margin of Gondwanaland. *Geologica Carpathica* 72 (6): 461–481. DOI: https://doi.org/10.31577/GeolCarp.72.6.2.

Morimoto N., Fabrices J., Ferguson A. K., Ginzburg I. V., Ross M., Seifer F. A., Zussman J., Akoi K., Gottard G. (1988) Nomenclature of pyroxenes. *Mineralogical Magazine* 52:535–550. DOI: https://doi.org/10.1180/minmag.1988.052.367.15.

Morley C. K., Kongwung B., Julapour A. A., Abdolghafourian M., Hajian M., Waples D., Warren J., Otterdoom H., Srisuriyon K., Kazeni H. (2009) Structural development of a major late Cenozoic basin and transpressional belt in central Iran: The Central Basin in the Qom-Saveh area. *Geosphere* 5:325–362. DOI: https://doi.org/10.1130/GES00223.1.

Mouthereau F., Lacombe O., Vergés J. (2012) Building the Zagros collisional orogen: timing, strain distribution and the dynamics of Arabia/Eurasia plate convergence. *Tectonophysics* 532:27–60. DOI: https://doi.org/10.1016/j.tecto.2012.01.022.

Nabatian G., Ghaderi M., Neubauer F., Honarmand H., Liu X., Dong Y., Jiang S. H. Y., Quadt A., Bernroider M. (2014) Petrogenesis of Tarom high-potassic granitoids in the Alborz-Azarbaijan belt, Iran: Geochemical, U-Pb zircon and Sr-Nd-Pb isotopic constraints. *Lithos* 184-187 (1): 324–345. DOI: https://doi.org/10.1016/j.lithos.2013.11.002.

Nabavi M. H. (1976) An Introduction to the Geology of Iran. *Geologic Survey of Iran, Tehran* 1976:109. In Persian

Nachite H., Ibhi A., Abia E. H. (2005) Discrimination between primary magmatic biotites, requilibrated biotites and neoformed biotites. *Comptes Rendus Geoscience* 337 (16): 1415–1420. DOI: https://doi.org/10.1016/j.crte.2005.09.002.

Nazari M., Arian M. A., Solgi A., Zareisahamieh R., Yazdi A. (2023) Geochemistry and tectonomagmatic environment of Eocene volcanic rocks in the Southeastern region of Abhar, NW Iran. *Iranian Journal of Earth Sciences* 15 (4): 228–247. DOI: https://doi.org/10.30495/ijes.2023.1956689.1746.

Ousta S. h., Ashja-Ardalan A., Yazdi A., Dabiri R., Arian M. A. (2024) Petrogenesis and tectonic implications of Miocene dikes in the southeast of Bam (SE Iran): Constraints on the development of active continental margin. *Geopersia* 14 (1): 89–111. DOI: https://doi.org/10.22059/geope.2023.364334.648729.

Ovung T. N., Ray J., Ghosh B., Koeberl C., Topa D., Paul M. (2018) Clinopyroxene composition of volcanics from the Manipur Ophiolite, Northeastern India: implications to geodynamic setting. *International Journal of Earth Sciences* 107:1215–1229. DOI: https://doi.org/10.1007/s00531-017-1529-y.

Pearce J. A. (2008) Geochemical fingerprinting of oceanic basalts with applications to ophiolite classification and the search for Archean oceanic crust *Lithos* 100 (1-4): 14–48. DOI: https://doi.org/10.1016/j.lithos.2007.06.016.

——— (1983) Role of the sub-continental lithosphere in magma genesis at active continental margins. *Continental Basalts and Mantle Xenoliths,* 230–249. https://orca.cardiff.ac.uk/id/eprint/8626

——— (1982) Trace element characteristics of lavas from destructive plate boundaries. *Orogenic andesites and related rocks, John Wiley and Sons,* 528–548. https://orca.cardiff.ac.uk/id/eprint/8625

Pearce J. A., Parkinson I. J. (1993) Trace element models for mantle melting: Application to volcanic arc petrogenesis, in Magmatic Processes and Plate Tectonics *Geolical Society Special Publication* 76 (1): 373–403. DOI: https://doi.org/10.1144/GSL.SP.1993.076.01.19.

Pearce J. A., Peate D. W. (1995) Tectonic Implications of the Composition of Volcanic Arc Magmas. *Annual Review of Earth and Planetary Sciences* 23 (1): 251–285. DOI: https://doi.org/10.1146/annurev.ea.23.050195.001343.

Peccerillo R., Taylor S. R. (1976) Geochemistry of Eocene calk-alkaline volcanic rocks from the Kastamonu area, northern Turkey. *Contributions to Mineral and Petrology* 58 (1): 63–81. DOI: https://doi.org/10.1007/BF00384745.

Poldervaart A., Hess H. H. (1968) Pyroxenes in crystallization of basaltic magmas. *Journal of Geology* 59:472–489. DOI: https://doi.org/10.1086/625891.

Rock N. M. S. (1991) Lamprophyres *Blackie* (Glasgow, Canada) 285

Rollinson H. R. (1993) Using Geochemical Data: Evaluation, Presentation, Interpretation. *John Wiley and Sons* 325 DOI: https://doi.org/10.4324/9781315845548.

Roohbakhsh P., Karimpour M. H., Shafaroudi A. M. (2018) Geology, mineralization, geochemistry and petrology of intrusions in the Kuh Zar Au-Cu deposit, Damghan. *Journal of Economic Geology* 10 (1) DOI: https://doi.org/10.22067/econg.v10i1.64316.

Roy A., Sarkar A., Jeyakumar S., Aggerawal K., Ebihara M. (2002) Sm-Nd age and mantle source characteristics of The Dhanjori volcanic rocks, Eastern India. *Geochemical Journal* 36 (5): 503–518. DOI: https://doi.org/10.2343/geochemj.36.503.

Rudnick R. L., Gao S. (2003) Composition of the Continental Crust. *Geochemistry* 3:1–64. DOI: https://doi.org/10.1016/B0-08-043751-6/03016-4.

Salehpour S., Arian M. A., Rad A. J., Zarei Sahamieh R., Yazdi A. (2025) Geochemistry and technomagmatic environment of Eocene volcanic rocks in Yuzbashi Chay region, west of Qazvin (Iran). *Iranian Journal of Earth Sciences* 17 (1): 1–13. DOI: https://doi.org/10.57647/j.ijes.2025.1701.04.

Saunders A. D., Storey M., Kent R. W., Norry M. J. (1992) Consequences of plume-lithosphere interactions. *Geological Society of Special Publication* 68:41–60. DOI: https://doi.org/10.1144/GSL.SP.1992.068.01.04.

Schandl E. S., Gorton M. P. (2002) Application of high field strength elements to discriminate tectonic settings in VMS environments. *Economic Geology* 97 (3): 629–642. DOI: https://doi.org/10.2113/gsecongeo.97.3.629.

Schmidt M. W., Jagoutz O. (2017) The global systematics of primitive arc melts. *Geochemistry, Geophysics, Geosystems* 18:2817–2854. DOI: https://doi.org/10.1002/2016GC006699.

Sepidbar F., Moghadam H. S., Zhangc L., Li J. W., Ma J., Stern R. J., Lin C. (2019) Across-arc geochemical variations in the Paleogene magmatic belt of Iran. *Lithos* 344-345:280–296. DOI: https://doi.org/10.1016/j.lithos.2019.06.022.

Smith E. I., Sánchez A., Walker J. D., Wang K. (1999) Geochemistry of mafic magmas in the Hurricane volcanic field, Utah: implications for small- and large-scale chemical variability of the lithospheric mantle. *Journal of Geology* 107:433–448. DOI: https://doi.org/10.1086/314355.

Soesoo A. A. (1997) Multivariate statistical analysis of clinopyroxene composition: empirical coordinates for the crystallization PT-estimations. *Geological Society of Sweden (Geologiska Föreningen)* 119:55–60. DOI: https://doi.org/10.1080/11035899709546454.

Speer J. A. (1984) Mica in igneous rocks. *Mineralogy, Mineralogical Society of America* 13:299–356.

Spies O., Lensch G., Mihm A. (1984) Petrology and geochemistry of the post-ophiolitic tertiary volcanics between Sabzevar and Quchan, NE Iran. *Neues Jahrbuch für Geologie und Paläontologie-Abhandlungen* 168:389–408. DOI: https://doi.org/10.1127/njgpa/168/1984/389.

Stöcklin J. (1968) Structural history and tectonics of Iran: A review. *Petroleum Geologists* 52:1229–1258. DOI: https://doi.org/10.1306/5D25C4A5-16C1-11D7-8645000102C1865D.

Sun S. S., McDonough W. F. (1989) Chemical and isotopic systematics of oceanic basalts: implications for mantle composition and processes. *Geological Society Special Publications* 42 (1): 313–345. DOI: https://doi.org/10.1144/GSL.SP.1989.042.01.19.

Taki S. (2011) Intrusives around Pirkooh village in western Alborz: an example of magmatic differentiation via fractional crystallization. *Journal of Earth and Resources* 4 (3): 11–19. In persian

Tatsumi Y., Eggins S. (1995) Subduction Zone Magmatism. *Blackwell Science,* 211.

Taylor S. R., McLennan S. M. (1985) The continental crust: its composition and evolution. *Geological Journal,* 312. DOI: https://doi.org/10.1002/gj.3350210116.

Tchameni R., Pouclet A., Penay J., Ganwa A. A., Toteu S. F. (2006) Petrography and geochemistry of the Ngaondere Pan - African granitoids in Central North Cameroon: Implication for their sources and geological setting. *Journal of African Earth Sciences* 44:511–529. https://insu.hal.science/hal-00073275

Teimouri S. S. (2011) Petrology and volcanic facies analysis in south of Jirandeh, East of Lushan, Northwest of Qazvin. *Ph.D thesis, Shahrood University of Technology, Shahrood, Iran*

Temel A., Gündoğdu M. N., Gourgaud A. (1998) Petrological and geochemical characteristics of Cenozoic high-K calc-alkaline volcanism in Konya, Central Anatolia, Turkey. *Journal of Volcanology and Geothermal Research* 85 (1): 327–354. DOI: https://doi.org/10.1016/S0377-0273(98)00062-6.

Turner S., Hawkesworth C., Gallagher K., Stewart K., Peate D., Mantovani M. (1996) Mantle plumes, flood basalts, and thermal models for melt generation beneath continents: assessment of a conductive heating model and application to the Parana. *Journal of Geophysical Research* 101 (B5): 11503–11518. DOI: https://doi.org/10.1029/96JB00430.

Upton P., Koons P. O., Phillips D. E. (2003) Extension and partitioning in an oblique subduction zone, New Zealand: Constraints from three-dimensional numerical modeling. *Tectonics* 22 (6): 1068. DOI: https://doi.org/10.1029/2002TC001431.

Verdel C. S., Wernicke B. P., Hassanzadeh J., Guest B. (2011) A Paleogene extensional arc flare-up in Iran. *Tectonics* 30 (TC3008) DOI: https://doi.org/10.1029/2010TC002809.

Vincent S. J., Allen M. B., Ismail-Zadeh A. D., Flecker R., Foland K. A., Simmons M. D. (2005) Insights from the Talysh of Azerbaijan into the Paleogene evolution of the South Caspian region. *The Geological Society of America* 117:1513–1533. DOI: https://doi.org/10.1130/b25690.1.

Wang D., Zhou J., Qiu J. (1991) The research status of shoshonitic series rocks. *Nanjing Univ (Earth Science)* 4:321–328.

Wang K. L., Chung A. S. L., Oreilly S. Y., Sun S. S., Shinjo R., Chen C. H. (2004) Geochemical Constraints for the Genesis of Post-Collisional Magmatism and the Geodynamic Evolution of the Northern Taiwan Region. *Journal of Petrology* 45 (5): 975–1011. DOI: https://doi.org/10.1093/petrology/egh001.

Whitney D. L., Evans B. W. (2010) Abbreviations for names of rock-forming minerals. *American Mineralogist* 95 (1): 185–187. DOI: https://doi.org/10.2138/am.2010.3371.

Wilson M. (1989) Igneous Petrogenesis. *Unwin Hyman, London,* 466.

Winter J. D. (2001) An introduction to igneous and metamorphic petrology. *Prentice Hall, New Jersey,* 697.

Xiao L., Clemens J. D. (2007) Origin of potassic (C-type) adakite magmas: experimental and field constraints. *Lithos* 95:399–414. DOI: https://doi.org/10.1016/j.lithos.2006.09.002.

Yazdi A., Shah Hoseini E., Razavi R. (2016) AMS, A method for determining magma flow in Dykes (Case study: Andesite Dyke). *Research Journal of Applied Sciences* 11 (3): 62–67. DOI: https://doi.org/10.3923/rjasci.2016.62.67.

Zhou Z. X. (1986) The Origin of Intrusive Mass in Fengshandong, Hubei Province. *Acta Petrologica Sinica* 2:59–70.